A NOVEL PRECLINICAL DUAL-TOPOLOGY MAGNETIC PARTICLE IMAGING SCANNER

A THESIS SUBMITTED TO
THE GRADUATE SCHOOL OF ENGINEERING AND SCIENCE
OF BILKENT UNIVERSITY
IN PARTIAL FULFILLMENT OF THE REQUIREMENTS FOR
THE DEGREE OF
MASTER OF SCIENCE
IN
ELECTRICAL AND ELECTRONICS ENGINEERING

By
Ahmet Rahmetullah Çağıl
December 2020

A Novel Preclinical Dual-Topology Magnetic Particle Imaging Scanner
By Ahmet Rahmetullah Çağıl
December 2020

We certify that we have read this thesis and that in our opinion it is fully adequate, in scope and in quality, as a thesis for the degree of Master of Science.

Emine Ülkü Sarıtaş Çukur(Advisor)

Ergin Atalar

Nevzat Güneri Gençer

Approved for the Graduate School of Engineering and Science:

Ezhan Karaşan
Director of the Graduate School

ABSTRACT

A NOVEL PRECLINICAL DUAL-TOPOLOGY MAGNETIC PARTICLE IMAGING SCANNER

Ahmet Rahmetullah Çağıl
M.S. in Electrical and Electronics Engineering
Advisor: Emine Ülkü Sarıtaş Çukur
December 2020

Magnetic Particle Imaging (MPI) is a relatively new biomedical imaging modality that can provide excellent sensitivity, contrast and resolution utilising superparamagnetic iron oxide nanoparticles. In MPI, spatial selectivity is achieved through selection fields created by either a permanent magnets or electromagnets. Selection fields generated by different arrangements of magnets result in different topologies of operation for MPI scanners. Among these scanner topologies, most prominent ones are Field Free Point (FFP) and Field Free Line (FFL) scanners, which differ in their advantages and disadvantages. Most importantly, FFL scanners provide improved sensitivity and rapid imaging, but offer only projection format images. FFP scanners offer 3D volumetric acquisition (and thus flexibility in acquiring an image from only a region or slice of interest), but can suffer from relatively lower sensitivity and longer scan times. In standard MPI scanners, as one topology has to be chosen when building a scanner, advantages of the other topology will be forgone. This thesis proposes a hybrid topology that functions as FFL by default, but can be swapped electronically into an FFP topology with the use of a saddle coil pair. This dual-topology scanner allows projection format images that can be used for rapid 2D projecton imaging or serve the purpose of a localizer, which can then be followed by 3D volumetric imaging of a region of interest. A preclinical hybrid scanner utilising the proposed topology is designed and constructed. Additionally, a novel double tuning mechanism that improves ease of tuning and allows for consistently achieving higher decoupling for gradiometer receive coils is introduced, built, and demonstrated.

Keywords: Magnetic particle imaging, dual-mode scanner, field-free point, field-free line, gradiometer receive coil.

ÖZET

ÖZGÜN BİR ÇİFT TOPOLOJİLİ KLİNİK ÖNCESİ MANYETİK PARÇACIK GÖRÜNTÜLEME TARAYICISI

Ahmet Rahmetullah Çağıl
Elektrik ve Elektronik Mühendisliği, Yüksek Lisans
Tez Danışmanı: Emine Ülkü Sarıtaş Çukur
Aralık 2020

Manyetik Parçacık Görüntüleme (MPG) süperparamanyetik demir oksit nanoparçacıkları (SPDP) kullanarak mükemmel hassasiyet, kontrast ve çözünürlük sağlayabilen nispeten yeni bir biyomedikal görüntüleme yöntemidir. MPG'de uzaysal seçiçilik sabit mıknatıslar veya elektromıknatıslar ile oluşturulan seçme alanları sayesinde sağlanır. Farklı mıknatıs yerleşimleriyle oluşturulan seçme alanları, MPG tarayıcıları için farklı çalışma topolojileri oluşturur. Bu farklı tarayıcı topolojilerinden en öne çıkanları, Manyetik Alansız Nokta (MAN) ve Manyetik Alansız Çizgi (MAÇ) tarayıcılardır. MAÇ tarayıcılar artırılmış hassasiyet ve hızlı görüntüleme sağlar, fakat sadece izdüşüm formatında görüntüleme imkanı sunar. MAN tarayıcılar 3B hacimsel görüntüleme (ve bunun bir sonucu olarak da sadece ilgilenilen bir bölgeden veya kesitten görüntü alma esnekliği) sağlar, fakat nispeten düşük hassasiyete ve daha uzun tarama sürelerine sahiptirler. Standard MPG tarayıcılarında, bir tarayıcı üretirken bu topolojilerden birinin seçilmesi gerektiği için, diğer topolojinin sunduğu avantajlardan vazgeçilmiş olunur. Bu tezde, varsayılan olarak MAÇ topolojisinde çalışan, fakat istenildiğinde elektronik olarak eyer tipi bobinler vasıtasıyla bir MAN tarayıcıya dönüştürülebilen hibrit bir topoloji önerilmiştir. Bu çift topolojili tarayıcı ile izdüşüm formatında hızlı 2B görüntüleme veya tek bir izdüşüm 'yerseyici' taramasının ardından ilgilenilen alandan alınacak bir 3B hacimsel tarama yapılabilir. Önerilen topolojiyi kullanan bir preklinik hibrit tarayıcı tasarlanmış ve gerçekleştirilmiştir. Ek olarak, gradyometrik alıcı bobinleri hassas ayarlamayı ve istikrarlı biçimde daha yüksek bağlaşım önleme elde etmeyi kolaylaştıran yeni bir çifte ayar mekanizması önerilmiş, geliştirilmiş ve gösterilmiştir.

Anahtar sözcükler: Manyetik parçacık görüntüleme, çift modlu tarayıcı, manyetik alansız nokta, manyetik alansız çizgi, gradyometrik alıcı bobin.

Acknowledgement

Due to my own areas of interest and the stuff I like to think and talk about, it was no surprise to me or anyone who knew me that I might work on a medical oriented subject that is also hardware-heavy in my graduate studies. However, it would surprise even me that this subject would be magnetic particle imaging because electromagnetics was never a strong suit of mine. In fact, it used to terrify me. The main reason I decided to work on MPI despite my fears and concerns was most definitely my supervisor Emine Ülkü Sarıtaş. Having taken two different courses of her before, I was already admiring how clear she always communicated her thoughts and how she approached her students with understanding and care. I felt I could take on all challenges of the graduate school with her guidance and come out stronger. And being under her supervision for three years only improved this impression. During this time, I went through many different problems, some related to my academic work and some related to my personal life. She helped not only with the former but also latter as well. She has been a great teacher, a great motivator, a great listener and a great inspiration. I feel very lucky to have worked with her and I will always remember how kind and thoughtful of a person she was. I am very thankful for her superb supervision.

I would like to thank Professor Ergin Atalar and Professor Nevzat Güneri Gençer, who, despite their undoubtedly busy schedules, spared time to be in my master's thesis committee.

I would like to thank the following funding agency for supporting the work in this thesis: the Scientific and Technological Research Council of Turkey through TÜBİTAK Grant 115E677 and Grant 217S069.

I would like to thank my mother and father, who first taught me what hardwork

looks like and what taking important responsibilites is. I am very glad that they have always been one to teach by showing, by example, and by leading the way. Without their example I would be far from the person I am today. Looking back to any achievement of mine that I consider a success, I see how their support was what made it possible. I still have a lot to learn about many intricacies of life from them, and I wish to always have them by my side.

I would like to thank my girlfriend, then fiancee and then wife, Şeyma. All of this work was possible through her endless encouragements and motivation. She has been the best companion I could hope for, replenishing my will to go on whenever I need it. I am extremely glad to have met her, and quite surprised at how quick and successful she was in transforming me from a careless, clueless kid to a responsible adult. She is the main reason I am excited about future, and I can't think of a life where I don't have her besides me.

I also would like to thank my friends at UMRAM who never spared their valuable time and effort whenever I asked for (and many times before I asked at all) any help, whether it was for my lab work, my course work or my personal life. Mustafa Ütkür was there to help with the scanner from day one, with the design as well as construction of it. He taught me how to use the 3D printer as well. Him and Ömer Arol both helped me push many of the magnets in place. Imaging simulations were possible thanks to Ömer Arol and Ecrin Yağız. Bilal Taşdelen carried many insights from the MRI world into our conversations. His strong work ethic was always an inspiration as well. Bilal and Ecrin were great listeners as well and I vented many of my frustrations as well as my excitements to them. Our walk in Central Park with Semih Kurt is a walk that I will always remember. Tunç Arslan's "Do you need help? I can help" attitude has saved many experiments from failing.

Contents

List of Figures

Chapter 1

Introduction

Magnetic Particle Imaging (MPI) is a relatively new biomedical imaging modality that promises high potential in spatial and temporal resolution, sensitivity and contrast [1]. MPI utilizes Superparamagnetic iron oxide (SPIO) nanoparticles as imaging tracers, which are shown be safe even for chronic kidney disease patients [2]. Some of the emerging applications of MPI are angiography, stem cell tracking, tumor imaging, and functional imaging [3][4]. As it is still a novel and rapidly developing modality, this list is sure to expand even further. SPIOs utilized in MPI have highly nonlinear magnetization responses. Their magnetization is linear for very small applied fields, quickly saturating when the field is increased beyond a certain threshold. As a result, a sinusoidal applied field with sufficiently large amplitude can periodically saturate the magnetization, creating harmonics of the excitation frequency in the received signal. These harmonics can then be used to measure the amount of magnetic nanoparticles within the excited volume. When an additional strong static field is introduced, particles can be made to remain saturated despite the sinusoidal excitation and thus be ‘silenced’. In MPI, this phenomenon can be exploited by selectively silencing all SPIOs except the ones in a Field Free Region

(FFR) by applying a Selection Field (SF). If the FFR is a point in space, it is called a Field Free Point (FFP). Only the particles that are within the FFP will respond to excitation with harmonics while the rest will be saturated and will not respond. By traversing this FFP in space, one can measure the amount of nanoparticles at the instantaneous position of the FFP, effectively acquiring a volumetric image of the magnetic nanoparticle density. If the FFR is in the shape of a line instead of a point, then it is called a Field Free Line (FFL). In the case of an FFL, sum of all responses from the particles along the FFL are obtained at once, which increases signal-to-noise ratio (SNR) and sensitivity. However, FFL can only be traversed along the plane perpendicular to itself, generating projection format images. By rotating either the FFL or the object of interest, one can acquire multiple projection images at different angles and create volumetric images via filtered backprojection reconstruction, as done routinely in Computed Tomography (CT). However, rotating the object can be undesirable (e.g., in the case of in vivo imaging) and rotating the FFL can be a challenging task in terms of hardware requirements. Furthermore, however small the region of interest may be, projection images from many different angles have to be acquired to reconstruct a volumetric image. In this thesis, a novel method for electronically transforming an FFL scanner into an FFP scanner utilising a saddle coil pair is proposed and an MPI scanner's design and construction from scratch is discussed and demonstrated to utilise the proposed method. With this dual topology scanner, it is possible to use projection imaging and volumetric imaging in conjunction. This may allow for a quick projection image to be taken as a localizer, which then may assist in defining a region of interest for volumetric acquisition. In addition, a novel doubly tunable gradiometric receive coil that aids in reducing interference in the receive chain by making it easier to tune is introduced, built and demonstrated.

Chapter 2

Background and Theory

2.1 Principles of Magnetic Particle Imaging

MPI relies on highly nonlinear magnetization response of SPIOs to image their spatial distribution in a region of interest [1]. Magnetization response of the SPIO nanoparticles can be modeled with the Langevin function shown in Figure 2.1. As can be seen in the figure, magnetization of the particles quickly saturate after a certain threshold. When a particle is saturated, it elicits almost no response to small variations in the magnetic field. This property is exploited to achieve spatial selectivity in MPI. A so called Selection Field (SF) is generated such that the particles are saturated everywhere but one point called the Field Free Point (FFP). When a sinusoidal excitation field is applied in addition to the SF, only the particles within the FFP respond to it, while the rest are saturated and therefore "silent". Then, the FFP can be steered within the volume to measure responses of particles and map these responses to the FFP position in space.

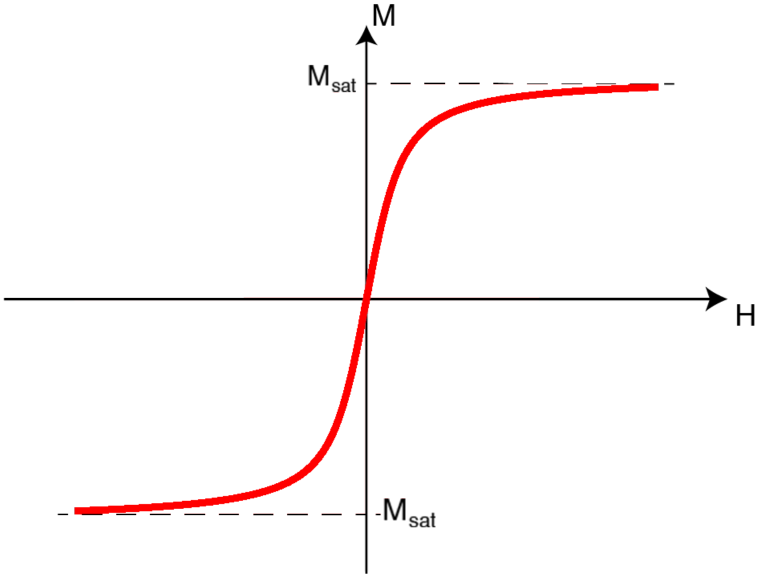

Figure 2.1: Langevin function used to model the nonlinear magnetization response of SPIO nanoparticles. External magnetic field is shown by the x-axis(H) and magnetization response of the nanoparticle is shown by the y-axis(M). Magnetization at which the saturation is said to occur is denoted by M_{sat}.

The above explanation can be clarified by explaining the mathematics of the principles for a simplified 1D case. Here, SF is denoted as $H_s(x)$, indicating that it is constant in time and only a function of space. Ideally, it changes linearly with gradient $-G$.

$$H_s(x) = -Gx \tag{2.1}$$

We can see that H_s is near zero only when x is near zero. In this configuration, the FFP lies at $x = 0$. Superposed on top of this field is $H_d(t)$, i.e., the drive field, which is a function of time and is usually a sinusoidal waveform. The position of the FFP can then be calculated by setting the total magnetic field to zero:

$$H_d(t) - Gx = 0 \tag{2.2}$$

$$x_s(t) = \frac{H_d(t)}{G} \tag{2.3}$$

In MPI, there are two major approaches to reconstructing an image from the acquired signal. One is System Function Reconstruction (SFR) and the other is X-Space reconstruction [5][6]. In SFR, the whole system is calibrated with a point source swept through all of the volume of interest. In X-Space approach, a more direct route is taken with the knowledge of FFP position and velocity.

1D Signal equation of the X-Space reconstruction was derived in [6]. The Langevin function describes the nonlinear magnetization of the SPIO nanoparticles as:

$$M(H) = m\rho\mathcal{L}(kH) \tag{2.4}$$

where $m\,[Am^2]$ is magnetic moment of the nanoparticle, ρ [particles/m^3] is density of nanoparticles, $k\,[m/A]$ is a property of the nanoparticles and $\mathcal{L}(\cdot)$ is the Langevin function. The magnetization can be rewritten as the following for 1D case:

$$M(x,t) = m\rho(x)\delta(y)\delta(z)\mathcal{L}[kG(x_s(t) - x)] \tag{2.5}$$

Equation 2.5 can then be converted to magnetic flux in the following way:

$$\phi(t) = m\iiint \rho(u)\delta(v)\delta(w)\mathcal{L}[kG(x_s(t) - u)]du\,dv\,dw \tag{2.6}$$

Then, Eq. 2.6 can be written as a convolution:

$$\phi(t) = m\rho(x) * \mathcal{L}[kGx]|_{x=x_s(t)} \tag{2.7}$$

Then, since the received signal is acquired from an inductive coil, the time derivative of the magnetic flux gives the signal equation:

$$s(t) = B_1 \frac{d\phi(t)}{dt} = B_1 m \rho(x) * \dot{\mathcal{L}}[kGx]|_{x=x_s(t)} kG\dot{x}_s(t) \tag{2.8}$$

where $-B_1\,[T/A]$ is the sensitivity of the receive coil.

2.2 Magnets and Selection Field

SF provides spatial selectivity in MPI by creating either an FFP or a Field Free Line (FFL). In an FFL topology, the received signal is the cumulative response of all particle responses within an entire line, as opposed to from just one point in space. Consequently, the spatial selectivity along the line axis is lost and the acquired image is no longer a volumetric image but a projection image. The advantage of the FFL topology is that it provides increased SNR since more particles are excited simultaneously [7]. Furthermore, imaging in projection format is significantly faster than 3D volumetric imaging.

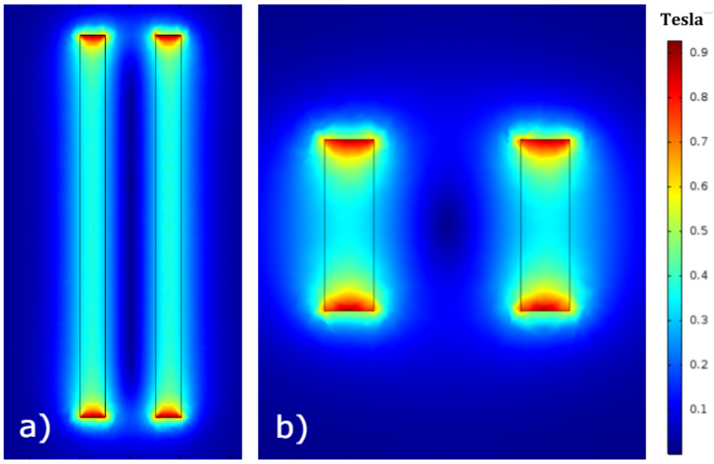

Figure 2.2: a) FFL selection field generated by an assembly of rectangular magnets. b) FFP selection field generated by a pair of cylindirical magnets (cross section through center is shown). (Magnitude of flux density is shown in both subfigures.)

SF can be generated either with permanent magnets or with electromagnets. Either choice has its merits and demerits, which are discussed briefly in Section 3.1. Unless otherwise mentioned, this thesis will assume that permanent magnets are utilized for generating the SF. In Figure 2.2, how an FFP and an FFL can be generated using permanent magnets is shown. In the case of FFP, two disk magnets with identical poles facing each other are placed with a gap distance. In the case of FFL, an array of rectangular magnets are utilised to create an elongated magnet structure on each side. This structure causes the FFP to be elongated, resulting in an FFL topology.

2.3 Scanner Body

As the magnets utilised in generating the SF apply enormous forces (in the orders of kilo Newtons) upon each other, they have a very strong tendency to not be stable in their intended positions. A body is required to hold the magnets safely and precisely in their positions. Using conductive materials for the body is not an option as the time-varying magnetic fields utilised in imaging can cause eddy currents within the body, interfering with the imaging signals. Likewise, using magnetic materials is not an option either, as they would change the shape of the magnetic fields and complicate the design process. A magnetic body would also make SF more susceptible to outside field perturbations [8]. Therefore, a non-conductive, non-magnetic and strong material has to be utilised in the design of the scanner body.

2.4 Shield

Even if the scanner body is built out of a non-conductive material, the generation of eddy currents is still a problem, as magnets themselves are conductive. Additionally, it is known that the magnetic field amplitude of permanent magnets depend on their temperature [8]. Since the eddy currents can cause heating within the magnets, shielding is crucial. To this end, a hollow copper cylinder (whose wall thickness is determined in Section 3.3) is inserted into the bore of the scanner. Then, the eddy currents will form on the copper shield instead of the magnets. Due to Lenz's law, these eddy currents will oppose the original time-varying field in direction, reducing the field amplitude experienced on the surface of the magnets, effectively shielding them [9]. As copper has very high thermal conductivity, heating is less of an issue for the shield as it performs as a moderate heatsink.

2.5 Transmit Coil

Transmit coil is the coil responsible for generating the time-varying magnetic field to excite the magnetic nanoparticles. It is a solenoidal coil that is excited sinusoidally, either in pulses or in a continuous manner. There are several requirements that drive its design in conflicting directions, creating trade-offs. First, it needs to generate a homogenous field to avoid artifacts such as fading, which requires the coil to be long [10]. However, it also needs to be power efficient to not melt its former (or itself, or harm the subject of the experiment), which in turn requires the coil to be short. Next, it needs to have high sensitivity to be able to generate the necessary excitation fields with the available current, but it also needs to have low inductance for ease of driving and to avoid high voltages across the coil. The design process of this coil is detailed in Section 3.4.

2.6 Tunable Receive Coil

In MPI, excitation and signal reception occur simultaneously, causing a Direct Feedthrough (DF) signal to form on the receive coil. This DF signal consumes most of the dynamic range available to the receive chain, as the signal received from the SPIOs are dwarfed by the magnitude of the DF. To deal with this problem, receive coils are wound in the so called “gradiometric configuration”. In this configuration, receive coil is wound in multiple segments with different winding directions [11]. The working principle here is that, given a sufficiently uniform distribution of transmit coil sensitivity, a coil with two segments which have equal number of turns wound in reverse directions should have equal voltages induced on each segment with opposing signs, effectively canceling each other. In such a configuration, a flux source can only be detected by the receive coil if it can induce a voltage on the receive coils in an asymmetrical manner. However, the most sensitive regions are the centers of each segment, which makes the 2-segment gradiometer coil inconvenient. However, the same principle can be applied to a three-segment receive coil, where the central segment is wound in one direction and the two side segments are wound in the opposite direction. In this configuration, turn counts are ideally given as N - 2N - N, where 2N corresponds to that of the central segment [12]. In Figure 2.3, a side by side comparison of sensitivity profiles of 2-segment and 3-segment gradiometer coils can be seen. In practice, however, since the excitation field is not perfectly uniform, the ratio of the central turn count to side turn count that yields the best decoupling will usually be less than 2. As it is quite challenging to know the excitation field profile perfectly beforehand and it is not entirely stable over time (e.g., due to changes in temperature or the positioning of the transmit coil), implementing a receive coil with a precomputed turns ratio may not provide the ideal decoupling of DF.

To overcome this problem, receive coils can be built such that they can be tuned after they are constructed [13]. Usually one of the segments is designed such that it can move along the bore direction. As the sensitivity of a transmit coil decreases away from the center, the compensation provided by the moving segment of the receive coil reduces as that segment is moved outwards. As a result, if the receive coil is initially designed with a slight overcompensation, it can be tuned successfully by carefully moving the free segment outward to a position that provides the highest level of decoupling. This approach is utilised in MPI spectrometers as well as MPI scanners.

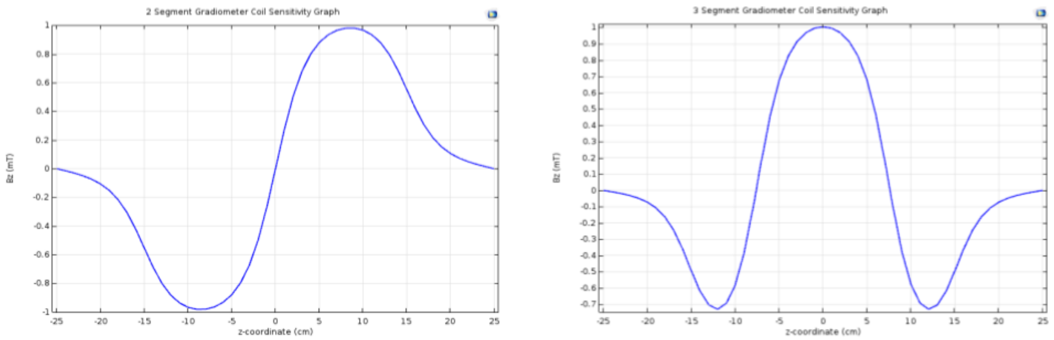

Figure 2.3: Left: Sensitivity profile of a 2-segment gradiometer coil. It has two maxima points which are equally sensitive, only differing in voltage direction. Right: Sensitivity profile of a 3-segment gradiometer coil. It has a single sensitivity maxima, which is conveniently located at the geometric center of the coil.

2.7 Electronics

In order to excite the SPIOs in the bore, transmit coil generates a time-varying magnetic field. To generate this magnetic field, a significant amount of AC current needs to be driven through the coil. Due to the dimensions and the high turn counts of the transmit coil, its inductance can approach mH range. Owing to this large inductance, even with a power amplifier capable of delivering few kilowatts of power, impedance matching between the amplifier and the coil becomes a necessity. This matching can be done with a matching circuit as simple as a series capacitor (or a very large capacitor bank in practice), but there are more sophisticated approaches with higher-order matching circuits or transformers as well [14]. Even though matching calculations are usually done with a target frequency in mind, in practice, it is hard to build a matching circuit that provides matching at the exact desired frequency when the capacitors have wide tolerances both in capacitance and in thermal stability. Instead, it is more practical to change the excitation frequency slightly after the the matching circuit is built and connected. (e.g., desired frequency may be 25 kHz, but matching may have occurred at 25.3 kHz due to tolerances of capacitors as well as minute effects unaccounted for in calculations such as the output impedance of an amplifier.)

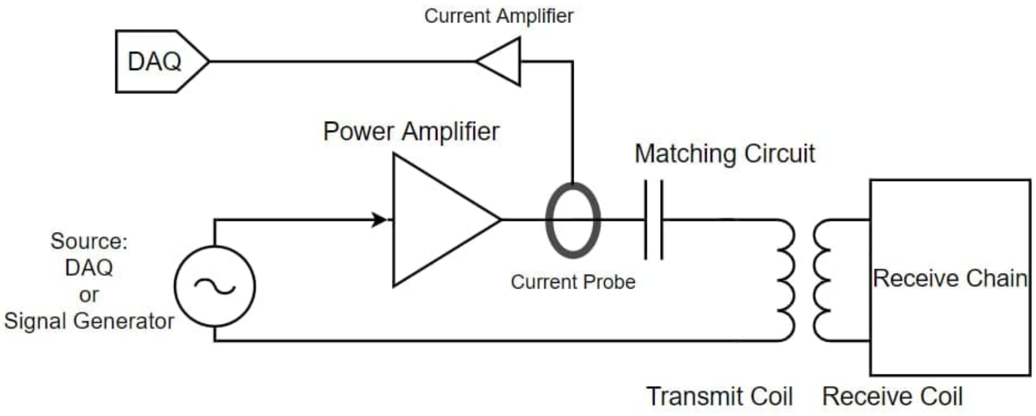

Figure 2.4: Overview of the transmit chain of a typical MPI system. A DAQ or signal generator is responsible for generating the excitation waveform. Generated excitation waveform is fed into a power amplifier. A matching circuit provides impedance matching between the amplifier and the transmit coil, it also removes any DC component of the signal. A Rogoswki current probe measures the current going through the transmit coil to make sure that the transmit coil has the intended current going through it, generating the desired field amplitude within the bore.

Once a current can be driven through the transmit coil at the desired frequency, a sinusoidal waveform at the desired frequency can be generated via a signal generator or digitally with a PC and a data acquisition (DAQ) device that combines both ADC and DAC functionality. In both cases, generated signal is fed into the aforementioned power amplifier, which is connected to the matched load. In Figure 2.4, an overview of transmit chain can be seen. A Rogowski current probe [15] provides feedback to ensure that the desired field amplitude is acquired within the bore.

On the receiving end (of which an overview is displayed in Figure 2.5), the receive coil is connected to a low noise amplifier to amplify the signal as much as possible without degrading the signal to noise ratio (SNR). If the DF is not sufficiently suppressed by the tunable receive coil, an analog notch filter designed to reject the DF frequencies may be employed between the receive coil and the low noise amplifier as well. However, using such a filter may not be desirable as it can cause a non-linear phase shift with respect to frequency, distorting the signal in time domain, and jeopardizing the success of the subsequent signal processing steps. Once the signal is amplified, it is fed into the DAQ to be sampled and stored in the PC for further processing.

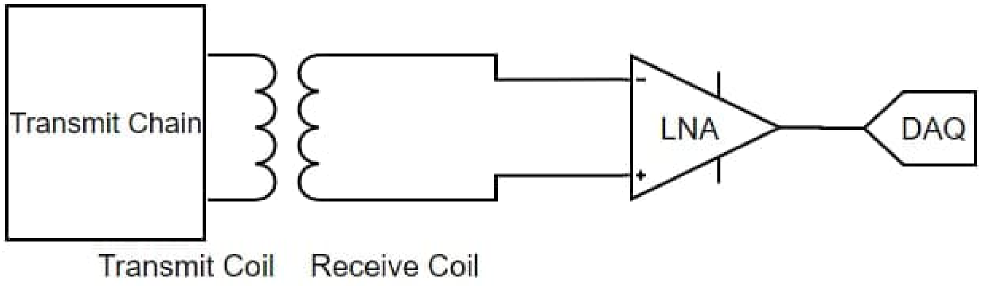

Figure 2.5: Overview of the receive chain of a typical MPI setup. A voltage is induced on the receive coil during the tranmission, which is amplified with a low noise amplifier, and then sampled via the DAQ. As the receive coil is usually configured gradiometrically, most of the direct feedthrough is eliminated even before the signal reaches low noise amplifier.

Chapter 3

Materials and Methods

This chapter is partly based on the publication titled ”A Preclinical Field Free Point/Field Free Line Hybrid MPI Scanner”, AR Cagil, EU Saritas, Proceedings of the 9th International Workshop on Magnetic Particle Imaging (IWMPI), 2019. It is also partly based on the publication titled “Design of a Doubly Tunable Gradiometer Coil”, AR Cagil, B Tasdelen, EU Saritas, Proceedings of the 10th International Workshop on Magnetic Particle Imaging (IWMPI), 2020.

Each component of the scanner goes through a design phase with different goals and constraints in mind. In this chapter, design process of each component is detailed. Details regarding the mechanical construction aspect of the scanner are omitted here and presented in Chapter 4.

3.1 Magnets and Selection Field

Usually, SF is generated by either two permanent magnets facing each other, or a pair of coils in Maxwell configuration. If generated by coils, SF constantly requires power to be enabled, whereas magnets provide this field with no power consumption. However, generating the field with magnets results in SF being permanent, and not being able to shut it down on demand may cause inconveniences. This trade-off scales with the volume and gradient of the field as well. A larger or higher gradient field will require more power or cause greater inconvenience. Additionally, an electromagnet will dissipate the required power as heat, which is another concern to manage. Considering that said inconveniences regarding the permanent magnet approach are expected to occur mainly during the construction phase rather than while using the scanner, the design of the MPI scanner proposed in this thesis chooses the permanent magnet approach for the SF.

As is customary from the magnetic resonance imaging (MRI) systems, we define the axis along the imaging bore to be the z-axis. The FFL lies on the y-axis, and the remaining axis perpendicular to both is the x-axis. With this coordinate frame, an FFL along the y-axis corresponds to a SF with the following gradient matrix:

$$G_{FFL} = \begin{bmatrix} -G_{zz}+\alpha & 0 & 0 \\ 0 & 0 & 0 \\ 0 & 0 & G_{zz}-\alpha \end{bmatrix}$$

As gradients play a determining role in the resolution of the system along different axes, it is desirable to have them be equal in magnitude (i.e., $\alpha = 0$), albeit not necessary. This point will be one of the driving factors in magnet design. Another factor is the resolution itself. We target a resolution of around 1 mm. As resolution depends on the intrinsic properties and diameter of the utilised nanoparticle [6], we assume a typical particle diameter of about 30 nm in calculations. The following formula describes the relationship among the intrinsic full width half max (FWHM) resolution of the MPI system, gradient strength, and particle diameter [6]:

$$FWHM \approx \frac{24k_BT}{\mu_0\pi M_{sat}}G^{-1}d^{-3} \tag{3.1}$$

Here k_B is the Boltzmann's constant, T is temperature, μ_0 is vacuum permeability, M_{sat} is a constant that is approximately equal to $0.6T/\mu_0$, G is the gradient strength of the SF and d is the nanoparticle diameter. This requirement necessitates that the gradients of the selection field be at least $4T/m$ in magnitude. Another design target is to enable preclinical animal studies, so the imaging bore needs to be wide enough to accomodate mice. Therefore, a free bore diameter of at least 30 mm is targeted. As three different coils and a shield should also fit between the magnets, we should leave plenty of gap space between the magnets (it is quite challenging to predict how much is required in advance, as it depends on the rest of the design). Another constraint is manufacturability. The magnets needed for an FFL scanner are very hard to come by in exact dimensions. Even when they are custom made, there is an upper limit to the dimensions of magnets. So these limitations must also be considered during the design process.

The above-mentioned targets and constraints are difficult to formulate as goals of an optimization algorithm. Therefore, the design process was performed manually, with iterations of finite element simulations of the field and gradients, followed by inspection.

Shown in Figure 3.1 is the finalised design for dimensions and placement of the SF magnets. Each magnet used is 152.4 mm × 101.6 mm × 50.8 mm in size. Five of them are stacked along their longest axis on each side of the magnet assembly. The distance between the magnet stacks is 100 mm. Simulation results of this magnet configuration are presented in Figure 3.2. As mentioned in Section 2.3, the scanner body to ensure safe and stable positioning of the magnets must be non-magnetic and non-conductive yet still very strong and durable. Therefore, an extremely strong glass-fiber compound material called G10 is utilised in the construction of the body. Further details of the body design and magnet assembly construction can be found in Chapter 4.

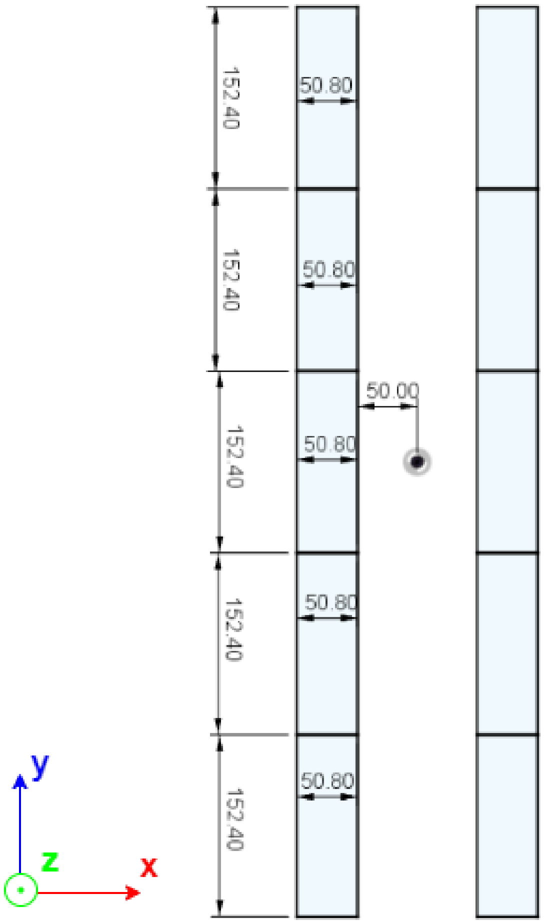

Figure 3.1: Finalized dimensions of the magnets and their placement. Depth in z direction is 101.6 mm.

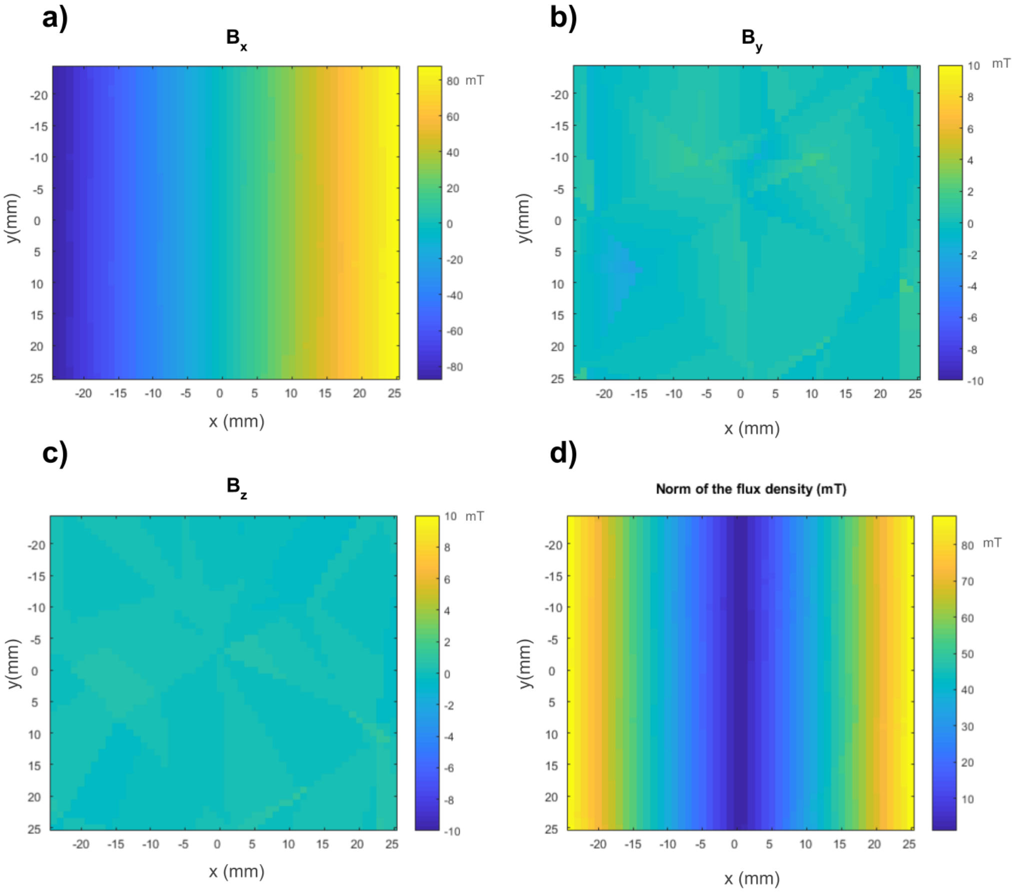

Figure 3.2: Simulated flux density within the bore in z=0 plane. a) B_x, b) B_y, c) B_z, d) The norm of the simulated B-field, where the FFL can be seen along the y-axis.

For measuring the flux density, a gaussmeter (LakeShore DSP 475) probe was fixated on a robot arm (Velmex X-Slide) using a custom 3D printed part shown in Figure 3.3, and both the robot arm and the gaussmeter was controlled via RS232 interface from MATLAB. The probe was positioned on each point of the grid to be sampled, with a 5-second pause to ensure that the gaussmeter reading settled. After the 5-second pause, the measured field was recorded into a matrix, and the probe was moved to the next position. Flux density measurements acquired from the z = 0 plane is shown in Figure 3.4. One can notice that y-axis and z-axis measurements are different than the simulation results. There are a few factors at play that contributes to this difference. One is the misalignment of the coordinate frames of magnet assembly and the robot arm. Another one is the misalignment of the probe itself (i.e., it is very challenging to ensure such a long probe's perpendicularity to the measured plane). However, this misalignment is not crucial for imaging.

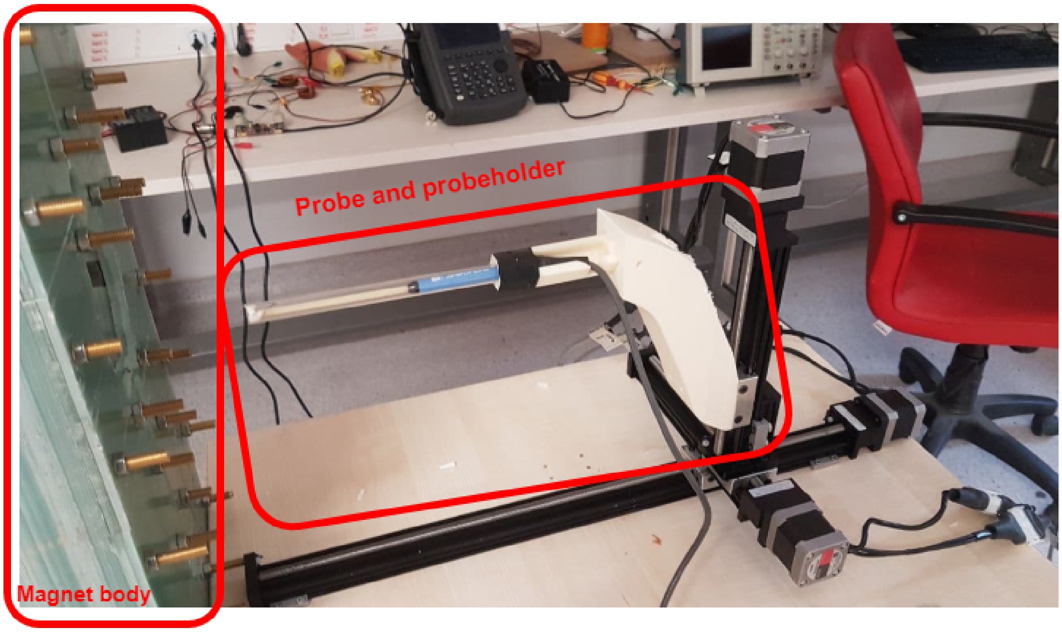

Figure 3.3: Custom 3D printed assembly that is used for holding the gaussmeter probes.

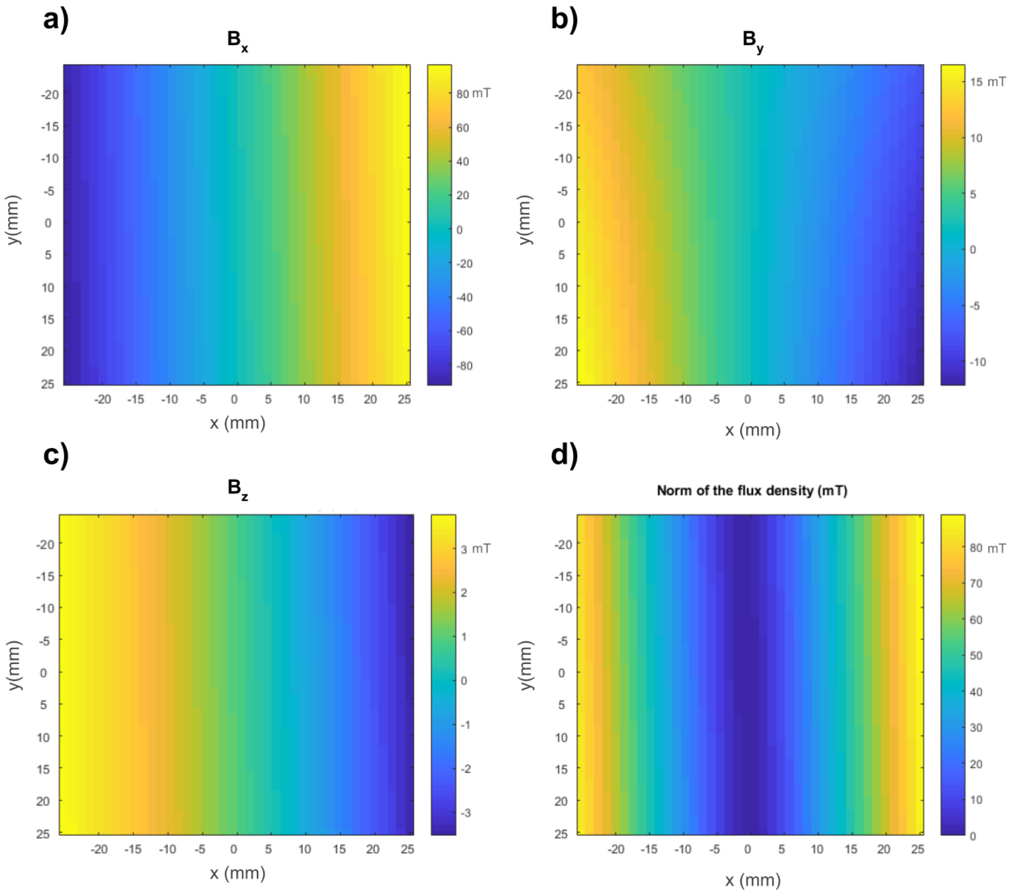

Figure 3.4: Measured flux density within the bore in z=0 plane. a) B_x, b) B_y, c) B_z, d) The norm of measured B-field, where the FFL can be seen along the y-axis.

3.2 Swap Coil

The swap coil that is proposed in this thesis is a saddle coil pair that generates a field such that, when superimposed with the existing FFL SF, yields an FFP SF. It accomplishes this task by providing the necessary constant gradient magnetic field along the direction of the FFL.

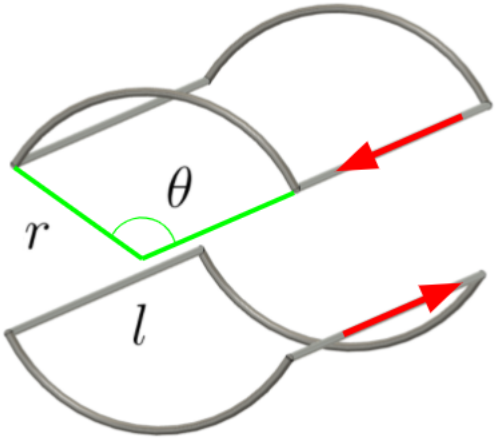

Figure 3.5: Saddle coil shape required to generate the necessary field for swapping an FFL into an FFP. Geometric parameters of the coil pair are shown on the coil. Also, current directions necessary to swap the FFL into an FFP are shown as well.

The Gradient matrix of the SF is characteristic for FFP and FFL modes. The following matrices apply for ideal FFP and FFL [7] [1]:

$$G_{FFP} = \begin{bmatrix} -G_{zz}/2 & 0 & 0 \\ 0 & -G_{zz}/2 & 0 \\ 0 & 0 & G_{zz} \end{bmatrix} \qquad G_{FFL} = \begin{bmatrix} -G_{zz} & 0 & 0 \\ 0 & 0 & 0 \\ 0 & 0 & G_{zz} \end{bmatrix}$$

To transform an existing FFL SF into an FFP SF, a swap field with gradient G_{swap} must be superimposed. The desired behaviour is:

$$G_{FFL} + G_{Swap} = G_{FFP}$$

This yields:

$$G_{Swap} = G_{FFP} - G_{FFL} =$$

$$\begin{bmatrix} -G_{zz}/2 & 0 & 0 \\ 0 & -G_{zz}/2 & 0 \\ 0 & 0 & G_{zz} \end{bmatrix} - \begin{bmatrix} -G_{zz} & 0 & 0 \\ 0 & 0 & 0 \\ 0 & 0 & G_{zz} \end{bmatrix} = \begin{bmatrix} G_{zz}/2 & 0 & 0 \\ 0 & -G_{zz}/2 & 0 \\ 0 & 0 & 0 \end{bmatrix}$$

The magnetic field with the gradient G_{swap} required to swap the FFL into an FFP can be provided by a pair of coils wound in a saddle shape, as shown in Figure 3.5

The standard parameters that need to be specified in designing any coil are wire diameter and turns count. In the case of a saddle coil, additional design parameters that describe the geometry of the coil are aperture radius r, aperture angle θ and coil length l. To generate a uniform gradient with a saddle coil, the following conditions must be met [16]:

$$\theta = \frac{2\pi}{3} \tag{3.2}$$

$$l = 4r \tag{3.3}$$

Therefore, as aperture angle is already fixed, fixing either the radius or the length defines the coil geometry in theory. However, in practice, as the coil will have some thickness due to winding of layers, calculations should take into account that r is the average radius of the swap coil. As the copper shield is designed to have a thickness of 5 mm (see Section 3.3) and that we desire a 15-mm radius for the free bore, the remaining radius available for the assembly of transmit coil, receive coil and swap coil is 30 mm at most. Knowing the ampere-turn requirement is important for deciding how much of this radius budget should be allocated to the swap coil. To determine the approximate ampere-turns necessary to swap the FFL into an FFP, a COMSOL (COMSOL AB., Stockholm, Sweden) simulation was run to calculate the sensitivity of the swap coil. A steady state problem was solved with the “magnetic fields” submodule of the AC/DC module. Since changing fields are not of interest for figuring out the sensitivity of the swap coil, it is not necessary to use the “magnetic and electric fields” submodule. The initial swap coil geometry used in the simulation can be seen in Figure 3.6. According to the simulation results, approximately 4000 Ampere-turns will be necessary. This value is bound to change slightly during the construction of the swap coil, due to potentially imperfect winding of the wires on such a challenging geometry.

Next to determine is the actual turn count and the operating current of the coil. As their product is set, determining one will set the other one as well. Here, the decision is driven mostly by practical concerns such as whether the existing amplifiers can supply the necessary current or whether one can wind the wire thickness implicitly chosen by the turn count. As the swap coil will be operated mostly in either DC or in very low frequencies, even though minimizing inductance is desirable, it is not a high priority concern.

In terms of practical concerns, the one that dominates the design is the windability of the coil. As the coil shape is complex, it does not allow the usage of usual tools and devices available for winding coils and therefore the process has to be handled with manual labor. Through several iterations of trial and error, a wire with 0.8 mm diameter was chosen as it provided a reasonable trade-off in ease of winding and number of turns (a thinner wire can be wound more easily but it increases both the risk of counting errors and the fragility of the entire coil). Next, to determine the turn count, one needs to target an approximate total cross-sectional area for the swap coil windings. Usually, to keep the ohmic heating manageable, a rule of thumb is to not exceed a current density of $5A/mm^2$ in copper wires. To stay at such levels of current density, keeping the approximately 80% packing factor of coil in mind,

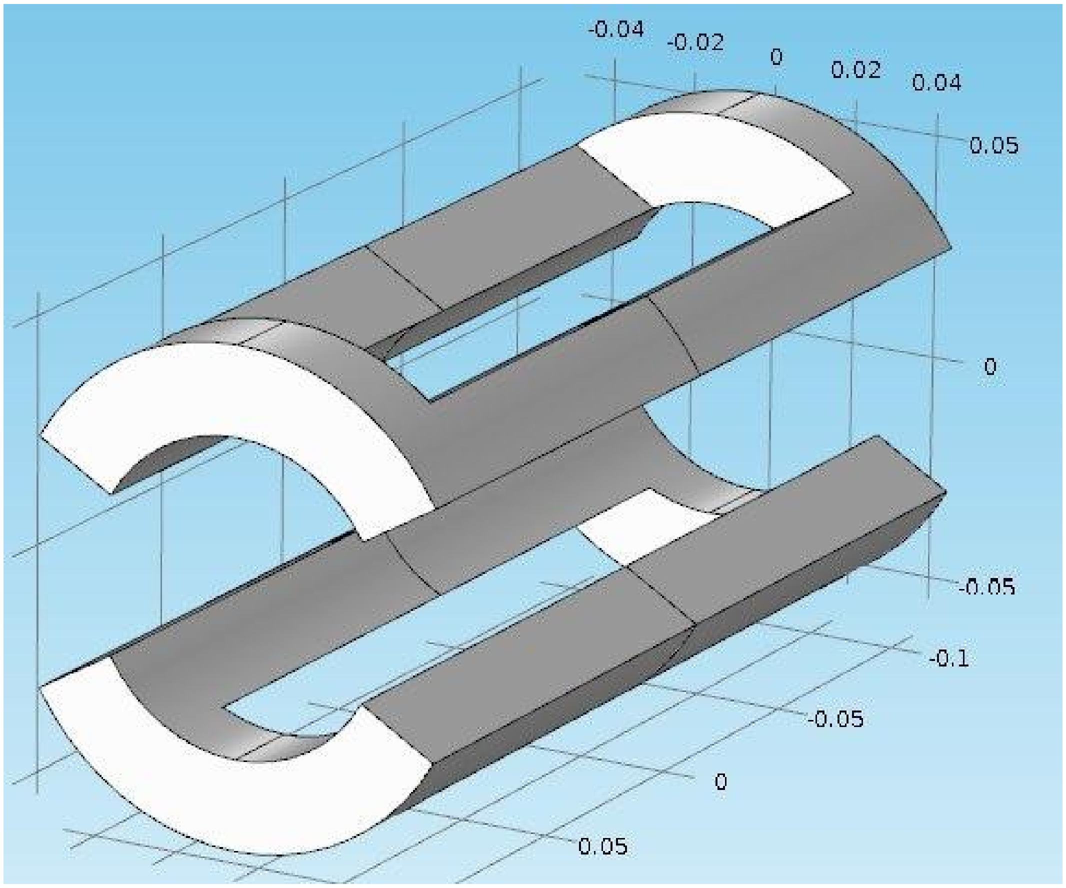

Figure 3.6: The initial swap coil geometry used in the simulation to assess the approximate ampere-turns necessary.

approximately 1000 mm^2 of cross-sectional area is required for the coil windings. In reality, however, at most one-tenth of this area can be allocated to coil windings, so that there is room left for the receive coil and the target 30-mm diameter bore. Therefore, to keep heating manageable, either active cooling has to be implemented or the swap coil needs to be operated in pulses to keep the average current density below the defined threshold in a periodic steady state. In the design of the MPI scanner proposed in this thesis, approximately 100 mm^2 of cross-sectional area was dedicated to the swap coil windings. In return, a pulsed operation with at most 10% duty cycle was targeted to compensate for the 10-fold reduction in the winding area. In Figure 3.7, gradient sensitivities calculated with the finalised parameters are displayed.

In Figure 3.8, the 3D model of the former that is designed to give the swap coil its shape and to hold it in place can be seen. Due to the complexity of the shape, it is hard to estimate the number of turns former can hold with precision. So, the design was 3D printed on an Ultimaker 3 3D printer, and the number of turns was determined by directly winding the coil on it. Several iterations of this process was realized to arrive at the latest design, which holds 125 turns of the 0.8 mm diameter wire. In theory, to achieve 4000 $Ampere - turns$, $32A$ of current needs to flow through this coil. It has a measured resistance of 3.75 Ω and an inductance of about 2.5 mH. The gradient sensitivity of the coil was measured (with a LakeShore DSP 475 Gaussmeter) to be 130 $mT/m/A$, indicating that $33.8A$ is needed instead of the previously approximated $32A$. Even though swap coil will operate at DC throughout the excitation and acquisition of signal, it will need to be pulsed with duty cycles lower than 10%. Therefore, the inductance of the swap coil is still relevant.

To drive a real (non-ideal) inductor in a pulsed manner, the voltage and current waveforms should be of the form in Figure 3.9. The initial spike in the voltage is needed to quickly ramp the current up to the desired level, and the following nonzero voltage is necessary to negate the negative voltage manifested across the

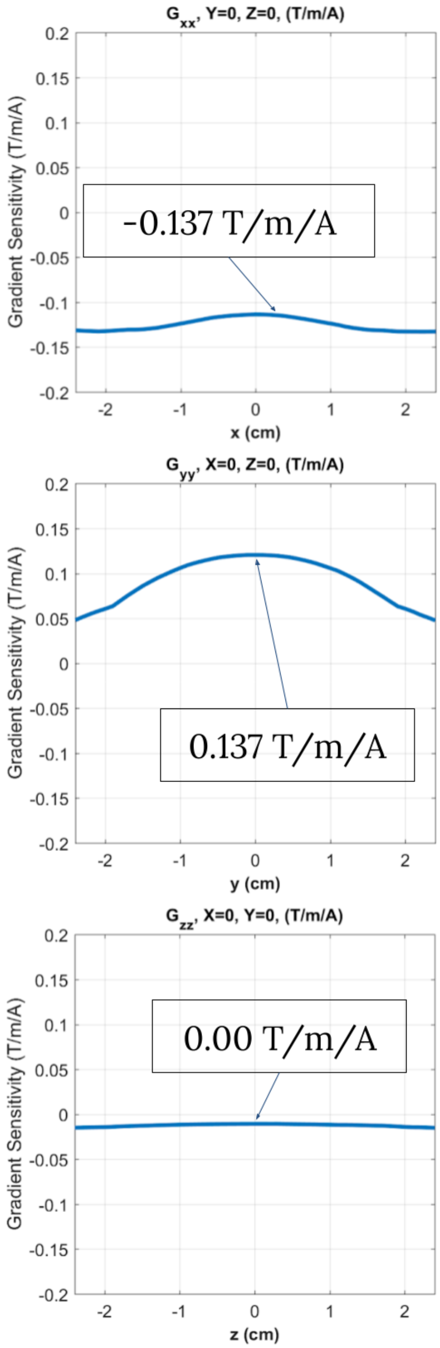

Figure 3.7: Gradient sensitivities calculated from the simulation results of the swap coil.

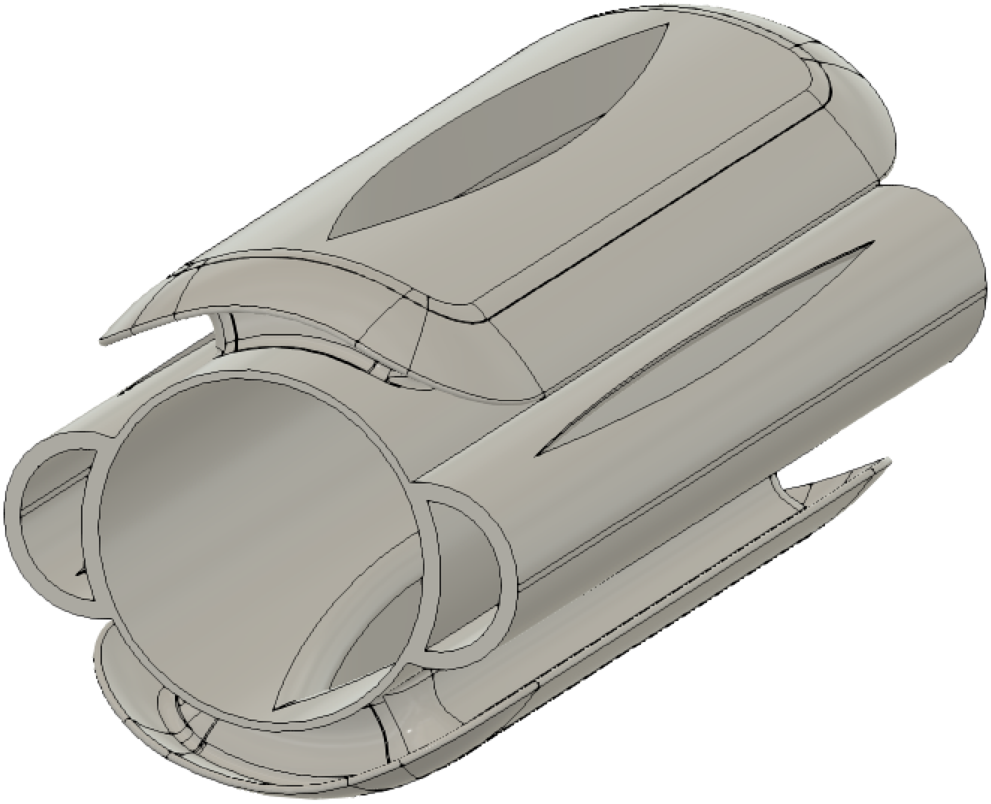

Figure 3.8: The former designed to hold the swap coil in place.

series resistance of the inductor. It can be deduced from the graph that, driving the coil with a square wave instead of a trapezoidal wave would result in an infinitely large voltage spike. Therefore, utilizing a trapezoidal waveform is necessary. The ramp-up time of the trapezoid depends on the maximum voltage that the amplifier can apply to the coil. The amplifier that will drive this inductor is AE-TECHRON 7796, which can, according to its datasheets, drive a 4 Ω load with 158 Volts across and 39 Amperes through [17]. Therefore, we can adjust the timing of the pulse such that it at most needs to apply 150 volts. In Figure 3.9, the rise and fall times are set to be 5 ms, which requires at most 135 volts across the coil at most for the current to rise to 32A. The fastest rise time that does not violate the 150V constraint is approximately 2.6 ms.

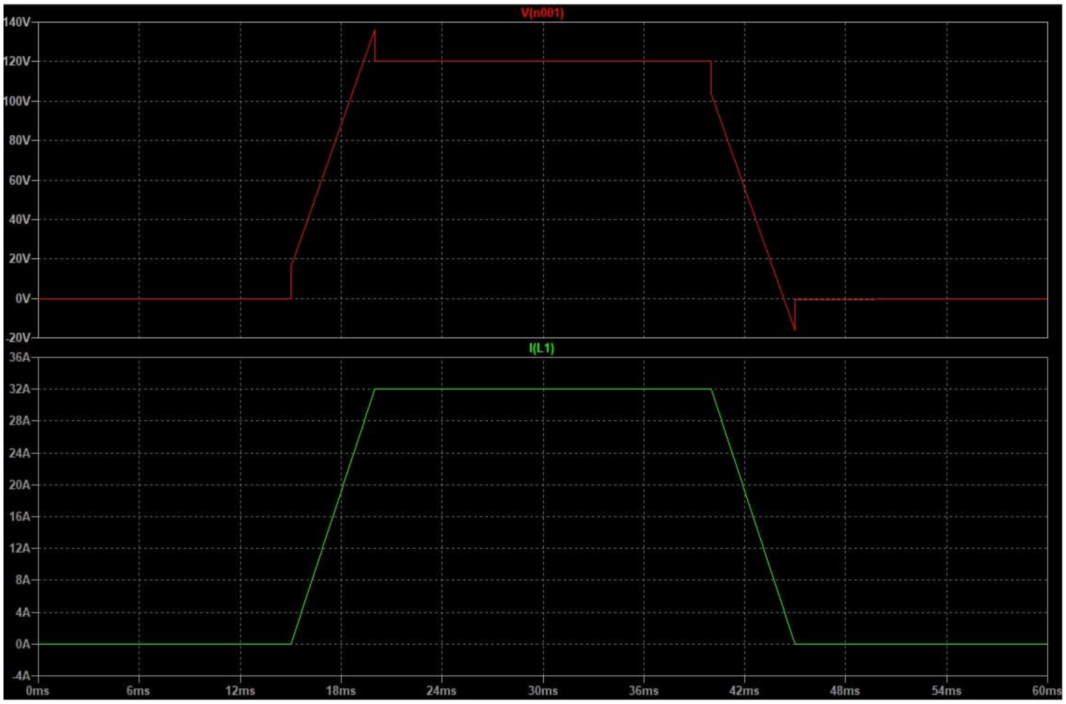

Figure 3.9: Top: Voltage waveform, Bottom: Current waveform

3.3 Shield

The copper shield is a hollow cylinder, with three important design parameters: length, outer diameter, and wall thickness. For the scanner proposed in this thesis, the outer diameter is set to 100 mm, which is the gap distance between the SF magnets. For the remaining parameters, there are opposing factors at play that drive the design. A longer shield is more effective, but limits access to the bore and becomes inconvenient to procure, machine, modify or handle in general. Furthermore, the improvements in the shielding effect becomes more and more marginal as the shield gets longer. A simulation study (frequency domain simulation of the transmit coil, shield, and magnets with the magnetic and electric fields submodule of the COMSOL) for different lengths of shields displays this diminishing returns effect in Figure 3.10. Due to both this effect and practical concerns such as material availability, the shield length was chosen as 156 mm.

Likewise, for the wall thickness of the shield, there are opposing factors at play. While increasing the wall thickness improves the effectiveness of shielding, there is a strong incentive to keep the shield as thin as possible due to the limited “radius budget” within the bore. One factor to consider here is the skin-effect. Alternating currents have a tendency to be distributed in an exponentially decreasing manner away from the surface of a conductor. This effect is called the skin effect and the depth at which the current density decreases to 1/e of its maximum value at conductor surface is called the skin depth. Accordingly, 95%, 99%, and 99.9% of the current flows within 3, 5, and 7 skin depths of a conductor, respectively. Hence, a wall thickness exceeding 6-7 skin depths can be considered as a waste of precious “radius budget”, as well as a waste of copper. Following formula is used to calculate the skin depth δ for a given conductor:

$$\delta = \sqrt{\frac{\rho}{\pi f \mu}} \tag{3.4}$$

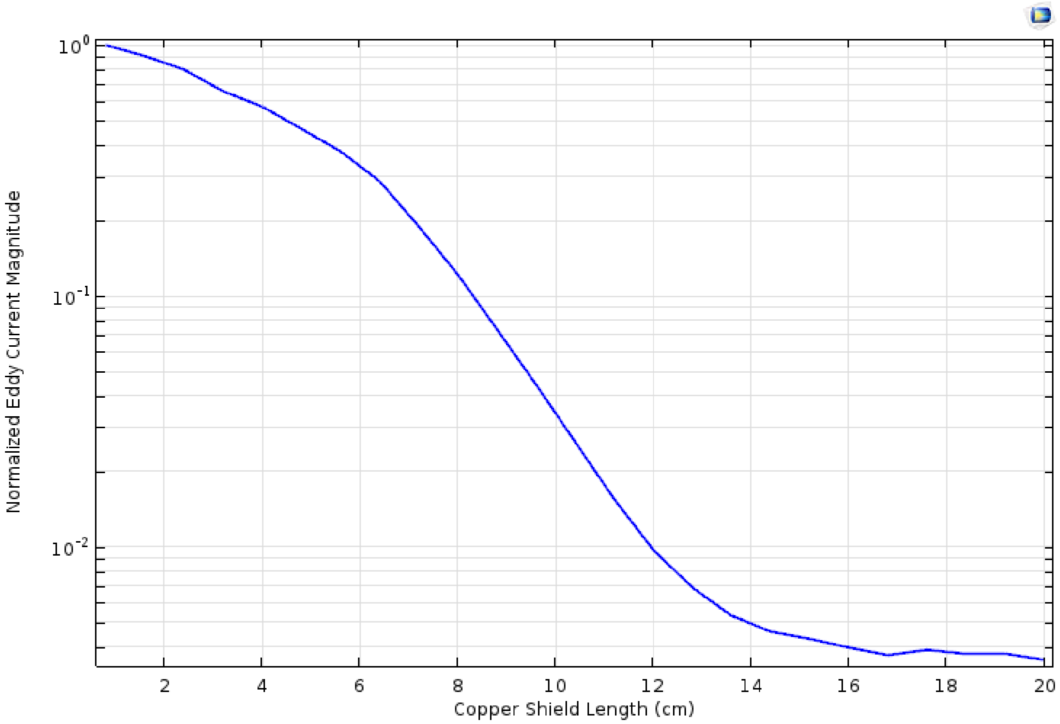

Figure 3.10: Eddy current induced within the center cross section ($z = 0$) of the entire magnet assembly, with respect to the length of the copper shield. Diminishing returns in the shielding effect can be observed. For these simulations, the outer diameter of the shield was 100 mm and wall thickness was 5 mm.

where ρ is conductivity, f is frequency in Hz and μ is the permeability of the conductor. Accordingly, the skin depths for copper at 5 kHz and 25 kHz are $934\mu m$ and $417\mu m$, respectively. Although the target transmit frequency for the proposed MPI scanner is 25 kHz, reserving the ability to operate at lower frequencies can allow the scanner to be used for relaxation mapping in MPI [18]. Therefore, the wall thickness was chosen as 5 mm, corresponding to more than 5 skin depths even at 5 kHz.

As the distance between magnets is 100 mm, once a copper shield of 5 mm thickness is inserted, the remaining bore radius is 45 mm.

3.4 Transmit Coil

The design of the transmit coil depends heavily on the design of the receive coil and vice versa, necessitating a simultaneous design of the two coils. To that end, a 2-D axisymmetric finite element model of the transmit coil, receive coil, and the shield together was created to simulate their interactions. While higher accuracy results could be obtained by modeling the entire scanner at once, the corresponding model would need to be 3D due to the non-axisymmetric nature of the SF magnets. Therefore, the resulting finite element simulations would be very demanding in terms of simulation time and computational resources.

The transmit coil needs to be able to excite the SPIOs with frequencies as low as 5 kHz and as high as 25 kHz. As the transmit frequency renders a single strand wire inefficient due to skin effect, the transmit coil needs to be wound using a Litz wire. For the transmit coil of the proposed scanner, a 1.25 mm Litz wire was utilized as it was readily available. With the wire diameter fixed, turn counts in a single layer of the coil determines the length of the coil, while the number of layers determines the thickness of the coil. Therefore, the design parameters that need to be chosen are the turn count, the number of layers, and either the inner or outer radius of the coil.

While positioning the transmit coil right inside the shield with an outer radius of 45 mm would be desirable considering the “radius budget”, it poses a detriment to the performance of the transmit coil. In such a case, the virtual coil that is produced by the induced currents on the shield mimic the sensitivity profile of the transmit coil very closely, resulting in a near perfect cancellation of the transmit field. The reduction in the effective sensitivity of the transmit coil makes it difficult to generate the desired field amplitudes within the imaging volume. If used in such a configuration, most of the transmit power is actually wasted on heating the shield and generating quite a high field within the tiny gap between the transmit coil and the shield. Allowing a gap between the transmit coil and the shield (i.e., decreasing the outer radius of the transmit coil) alleviates this effect with a minor reduction in shielding efficacy.

Therefore, in the final design, the outer radius of the transmit coil was chosen as 40 mm (i.e., 5-mm gap between the shield and the coil), with 3 layers of windings. Allowing a gap increases the sensitivity of the transmit coil. The turn count was determined to be 240, distributed in 3 layers of 80 turns each, and accordingly the length was 96 mm. The sensitivity of the final coil was measured with a LakeShore DSP 475 Gaussmeter along the z direction and was found as 1.37 mT/A at scanner isocenter. After the coil was constructed, its DC-resistance and inductance was measured with a precision LCR meter (GW Instek LCR-8105 G), and found as 2.78 Ω and 738 μH, respectively.

3.5 Matching Circuitry

A matching circuit fulfills two roles in the transmit chain. One is its primary role, which is to match the transmit coil to the desired drive frequency. And the second role it fulfills, even though it is not necessarily intentfully designed for it, is to block any DC component of the transmit coil's driving current. This second role is not a design necessity, as the driving current is not supposed to have a DC component anyways, but it is more of a bonus safety feature that comes with using series capacitors to match the coil to the desired driving frequency. It is a safety feature because, if for any reason a DC current flows through the transmit coil, due to the extremely strong magnetic field it resides in, it transforms into a projectile magnetically launched along the bore direction. With the caveat out of the way, we can consider the design of the matching circuit.

When matching an inductor to a single frequency, the goal is to make the load appear solely resistive. As the inductor in question is a real inductor with nonzero series resistance built into it, the real part of its impedance can not be lowered below the series resistance of the inductor's wire. Jacobi's law (Maximum Power Transfer Theorem) dictates that maximum power transfer occurs when the load impedance is equal to the complex conjugate of the source impedance. However, in our context, real part of the load impedance (measured as 2.78 Ω in Section 3.4) is significantly larger than the source impedance of the amplifier used to drive the transmit coil(5.3 $m\Omega$ and 0.95 μH for AE- Techron 7224) [19]. Therefore, best we can do in this scenario is to reduce the imaginary part of the impedance to zero. For that end, a series capacitor (56nF for our load) chosen according to a very trivial phasor domain calculation should be enough.

However, unfortunately, the capacitor to be used is also real, just like the coil, and therefore comes with its own complications. Two main problems arise. One is that, many $kiloVolts$ (3.6 kV_{pp} in our case) of potential may develop over the inductor and over the capacitor. Second one is that, the capacitor has its own equivalent series resistance (ESR), which causes it to heat as the AC current goes back and forth through it. Several measures can be applied to mitigate these problems. One is to select the capacitors carefully so that they can withstand high AC voltages and they have low ESR. Another measure is to first put the capacitors in series so that they share the high voltage difference across many of them. By putting them in series, the voltages they have to withstand decreases, however, equivalent capacitance also decreases as well. So, to compensate for the decreasing capacitance, several of these series capacitor banks should be connected in parallel. So, if a capacitance of x Farads is needed and we do have an x Farad capacitor to begin with, and we need to divide the voltage across n of these capacitors in series, to compensate, we need n branches of the series banks. Therefore, we need n^2 identical capacitors to build the capacitor bank. In Figure 3.11, comparison of an ideal scenario and a practical realization of it can be seen. Our realization had n=7.

3.6 Receive Coil

As explained in the background section, to eliminate DF in MPI, the receive coil has to be in the form of a gradiometer. In the ideal design of a gradiometer receive coil where the transmit field is uniform over the entire space, it is trivial to calculate the turn counts necessary to make the gradiometer work. However, in a realistic design space, the exact design of the gradiometer is extremely dependent on the shape of the transmit field. To be able to compensate any errors and minute unaccounted effects in computation, we wish to design this gradiometer to be tunable. Furthermore, to aid in tuning process, we design it to be doubly-tunable as a novel contribution. In this case, the transmit coil and the doubly tunable gradiometric receive coil must be designed in tandem. As mentioned before, this was accomplished by creating a simulation environment where transmit coil, receive coil and the copper shield is all modeled together, (with mesh resolution as low as 10 μm due to the high precision nature of the receive coil, as will be apparent in the rest of this section) complicating the simulation process.

Before moving on with the details of the simulation, workings of the doubly tunable gradiometric receive coil has to be explained.

A gradiometric receive coil works by cancelling out any source of induction that affects the entirety of the receive coil homogeneously, and only letting local sources to induce any voltage on the coil [12]. An explanation of how this works was made in Section 2.6. A tunable gradiometric receive coil builds on this idea by making one of the segments of the gradiometer movable in one axis [13]. Being able to move the segment allows one to control the amount of contribution that segments makes, so that minor changes in environment or any unwanted bias in the decoupling can be tuned out to some degree.

One of the problems faced while using a tunable gradiometric coil is that, as the decoupling approaches the optimal decoupling, it gets harder to tune because the optimal decoupling region is very narrow. A depiction of this can be seen in Figure 3.12. In the span of half a millimeter, 30 dB of decoupling is gained and lost again. Depending on how quickly the segment was moved, the point of optimal decoupling may even go unnoticed. Even the use of a fine pitched screw to help position the segment can not entirely mitigate this problem.

This problem occurs because the plot is too steep. Changes in DF magnitude happen too quickly with respect to the tuning position, i.e., the tuning sensitivity is too high. A lower tuning sensitivity achieved by a smaller turn count would help solve this problem, but then the range of tuning would decrease, creating another problem. The solution this thesis proposes is to combine the two ideas and have two different tuning coils where the high sensitivity, high turn count segment provides the wide range and the coarse tuning ability, and the low sensitivity, low turn count segment provides a finer tuning ability in a narrower region. To achieve this mode of operation, however, the fine tuning segment has to be the one further away from the central segment. Otherwise, there may occur scenarios where fine tuning segment actually has higher sensitivity than the coarse tuning segment. Another guarantee that has to be provided is that, any positional change made to coarse tuning segment should also apply to fine tuning segment, i.e., the coarse tuning screw should move both the coarse and fine tuning segments, but fine tuning screw should only move the fine tuning segment. How this is achieved in practice is detailed in Section 4.5.

When above mentioned two guarantees are provided, a 2D sweep of tuning segment positions can be done in simulation to achieve a “valley plot” like the one shown in Figure 3.13. This plot shows the magnitude and sign of the voltage induced by DF, as a function of the positions of tuning segments. Figure 3.12 can be thought of as a cross section of this “valley plot”. In the context of achieving a high decoupling, we want to configure our receive coil such that it operates anywhere on the white line in the center of the plot. That line is where the zero crossover of the DF happens, so the minimum DF is also on that line. This plot also reveals the previously mentioned problem of decoupling region being too narrow. Notice how narrow, in horizontal direction, the bright region is, and compare it with how wide the same region can be in the vertical direction. Also notice how different the scaling of the axes are. In Figure 3.14, the same valley plot is displayed, only colored by discrete steps of 20 dB decoupling, such that blue region indicates decoupling greater than 40 dB, red region indicates decoupling greater than 60 dB and green region indicates decoupling greater than 80 dB. In this plot, we can easily see that the width of the green region measures approximately 20 μm in horizontal direction and approximately 1400 μm in vertical direction. The latter is certainly a more achievable tuning target.

“Valley plot”s above aided significantly during the design of the doubly tunable gradiometric receive coil, however, the optimal decoupling was only part of the picture. Another concern is the sensitivity profile of the receive coil. Care should be taken in the design to make sure that the expected optimum point occurs relatively close to the point where neither of the coils has moved away, so that the sensitivity profile is not skewed to one side and is as homogenous as possible. To manage this, the fixed segment of the gradiometric coil needs to be positioned a few mm’s away from the central segment, so that the tuning operation does not skew the sensitivity profile dramatically. This also has the added benefit of easing the winding process of the coil.

With these principles in mind, the actual design process consists of many runs of simulations with manual parameter search in between. As the transmit coil, the receive coil, and the shield is modeled together, all of their parameters were tweaked simultaneously to arrive at a design that satisfies all the needs previously mentioned within this thesis. We settled at the dimensions and turn counts displayed over the receive coil former in Figure 3.15. A 36-mm coil diameter allows for mice to be inserted inside the bore, and a 50-turn central segment provides the sensitive region.

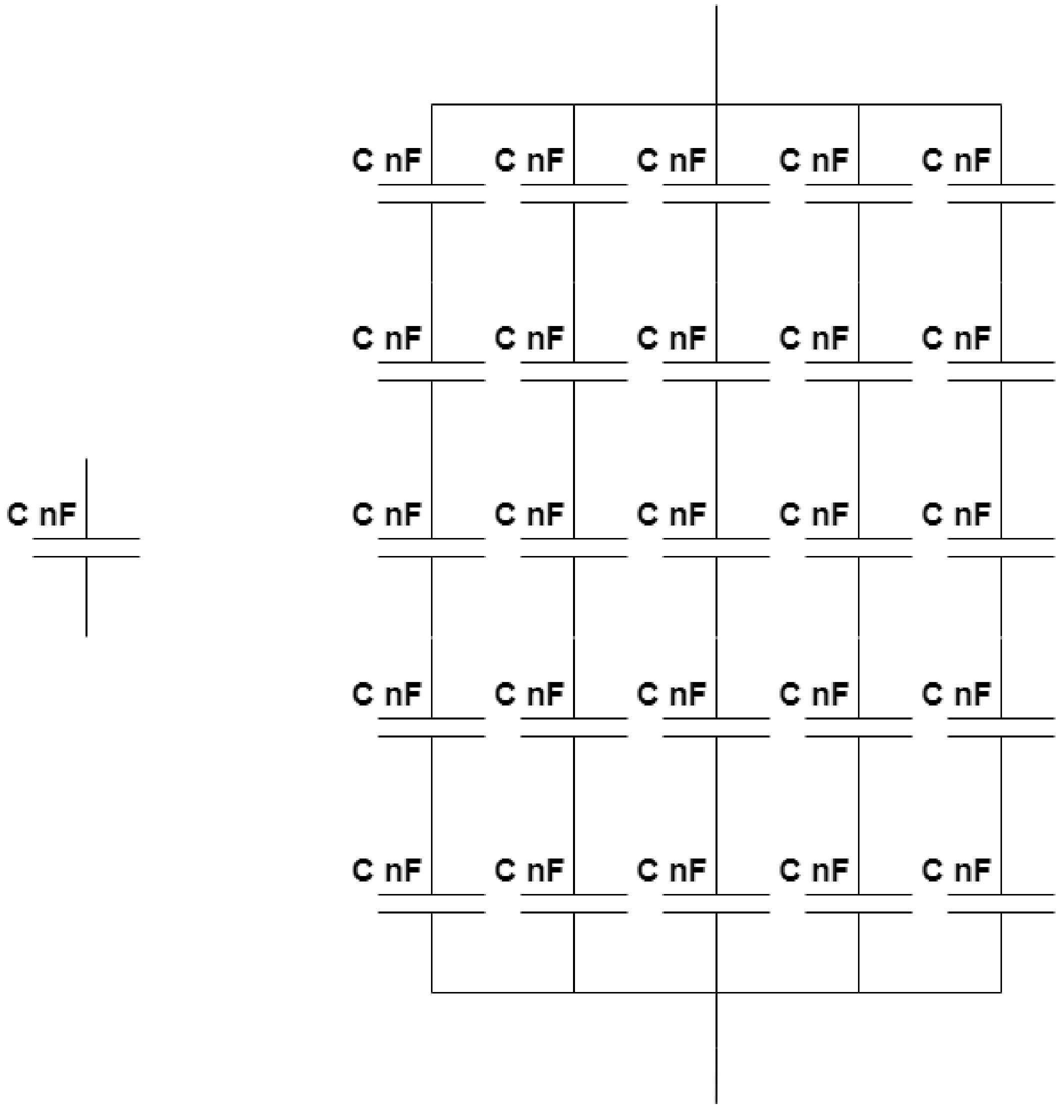

Figure 3.11: Left: Ideal capacitor used for matching. Right: A typical n × n capacitor bank that needs to be used for matching in practice.

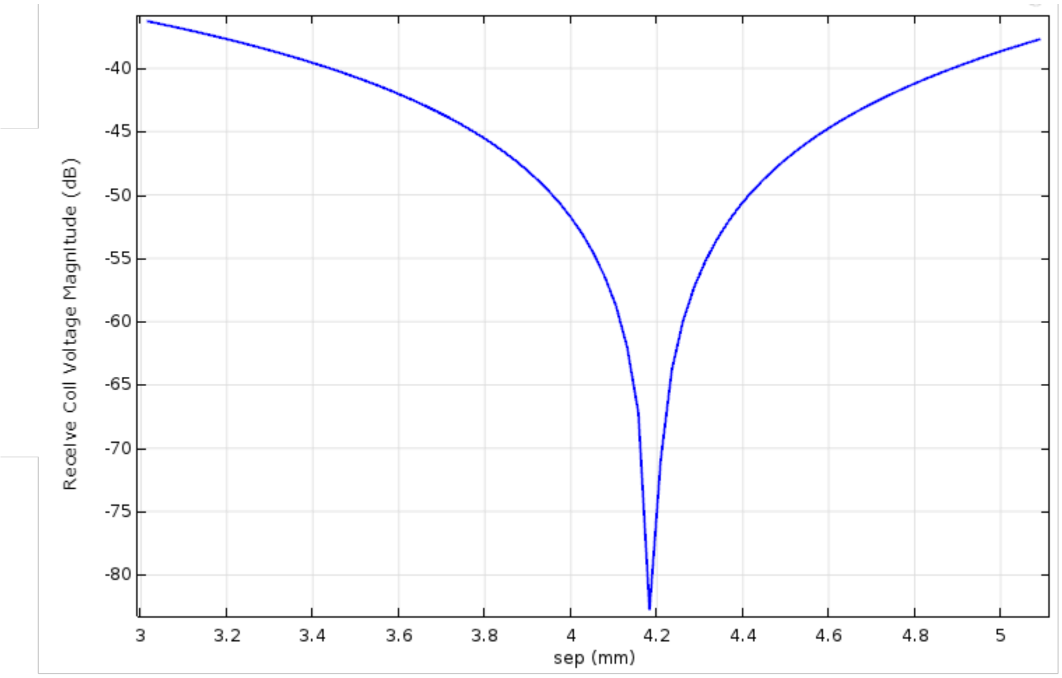

Figure 3.12: Direct feedthrough magnitude as a function of tuning segment's position. The variable *sep*, shown on x-axis, is the separation between the moving tuning segment and the static central segment of the receive coil. On y-axis, magnitude of the direct feedthrough induced on the receive coil is plotted in decibels.

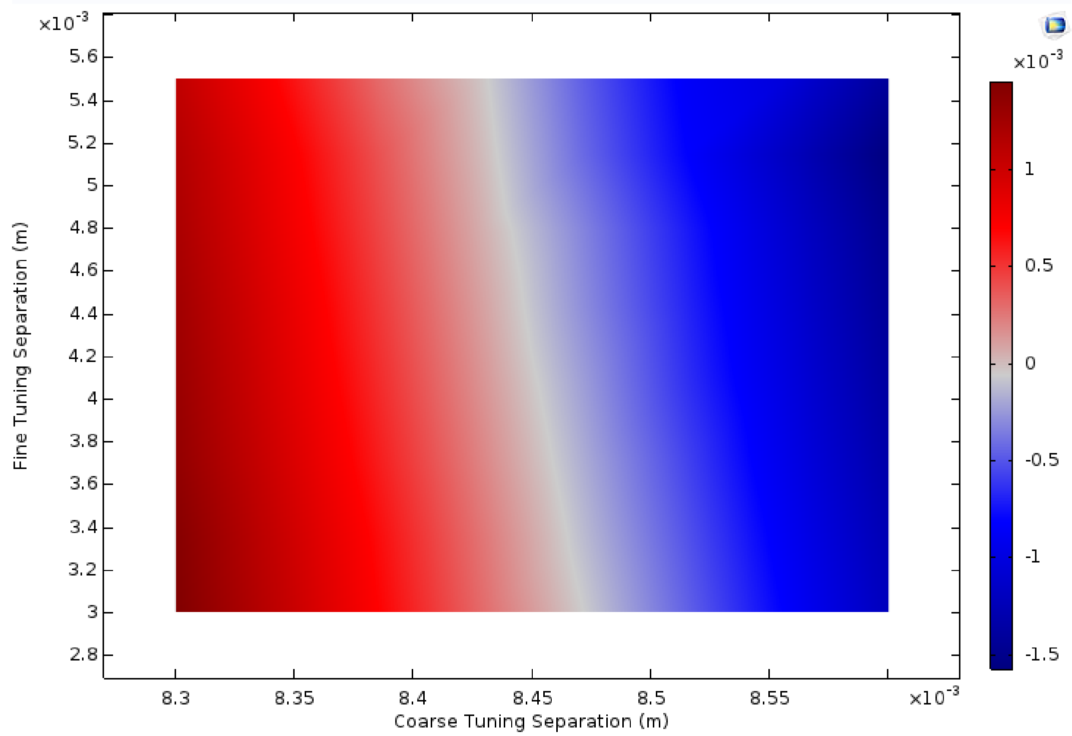

Figure 3.13: Valley plot: Magnitude of the voltage induced by DF as a function of the positions of the tuning segments. Notice the dramatic difference in scales of the axes. Due to such a great difference, it is not practical to display this plot in equal axis scaling.

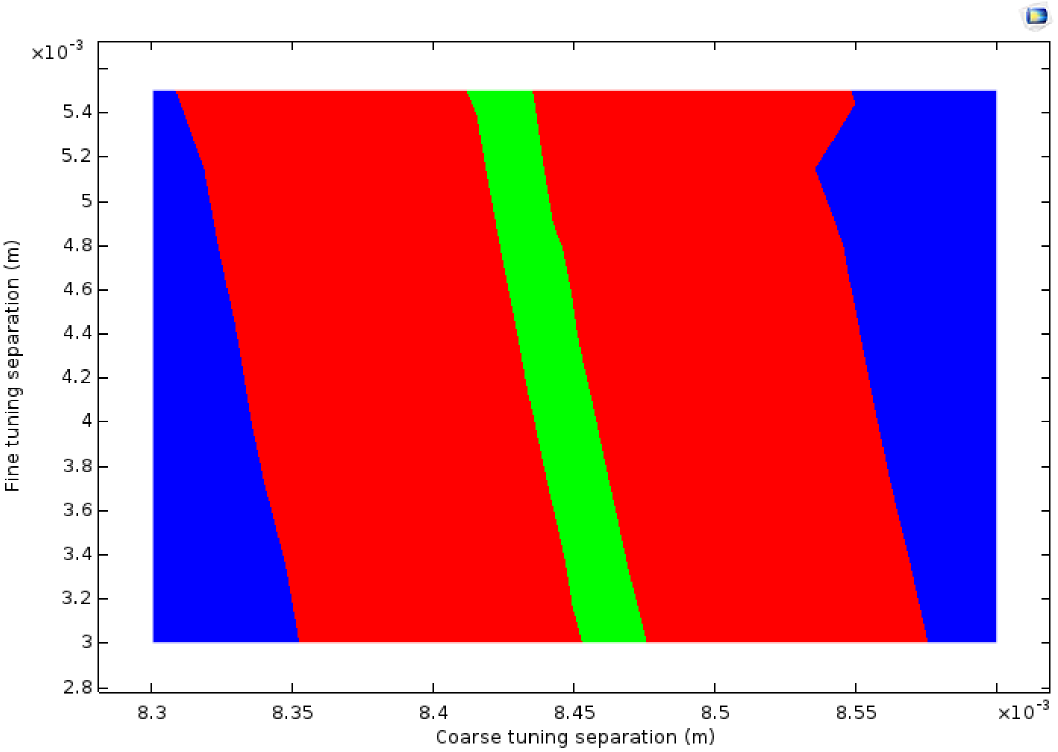

Figure 3.14: Magnitude of the voltage induced by DF as a function of the positions of the tuning segments, plotted in 20 dB wide steps to clearly reveal the difference in cross section widths across horizontal and vertical axes.

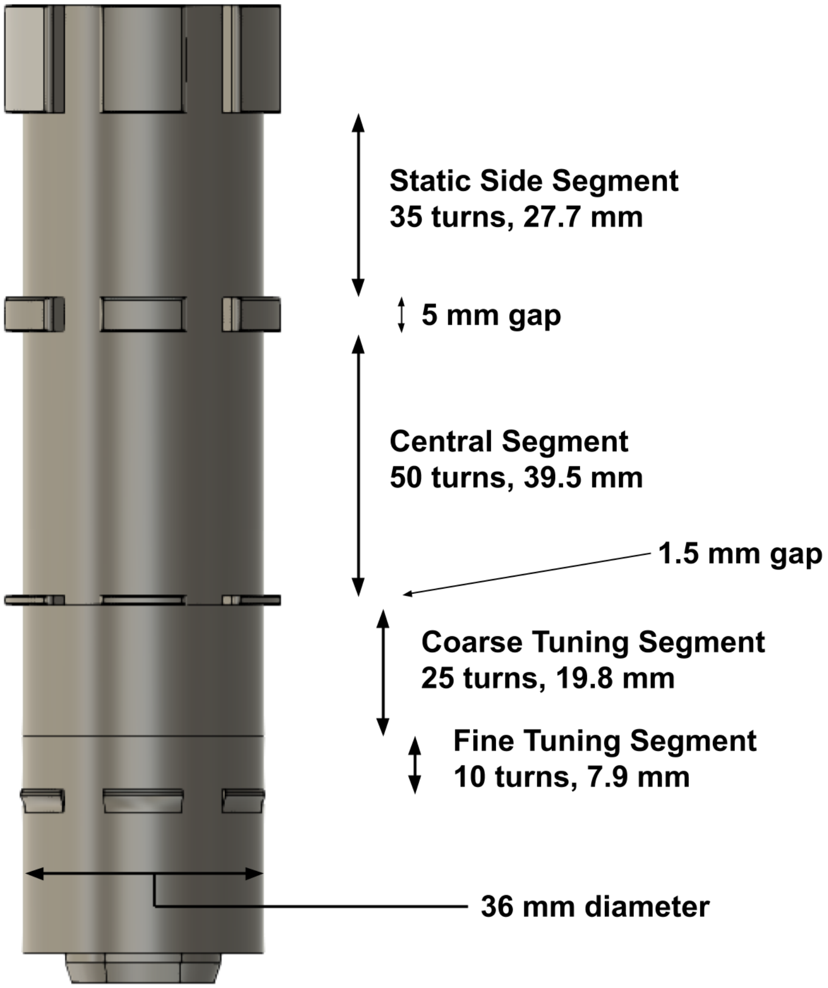

Figure 3.15: Final design parameters of the receive coil, displayed on their respective locations over the coil former.

Chapter 4

Construction Details

4.1 Scanner Body

In Section 3.1, the positioning of the permanent magnets were described. With North poles facing each other, the magnets on both sides push each other away from the center of the scanner. Furthermore, magnets on the same side push each other in upward and downward directions, as well. As the magnets are large in size, the resulting forces are quite strong. A simulation in COMSOL reveals that the expected forces the scanner body must withstand are in the ballpark of 2500 Newtons. The design of the body was performed by inputting the results from the magnetic simulation in COMSOL to a static load analysis simulation in Fusion 360. In Figure 4.1, the starting point of the design can be seen alongside the final design. First, the weak points of the initial design was determined by applying the expected load in simulation, and then these points were reinforced to arrive at the final design. In the final design, a safety factor greater than 6 is achieved, that is, the resulting structure is computed as 6 times stronger than the loads it has to endure.

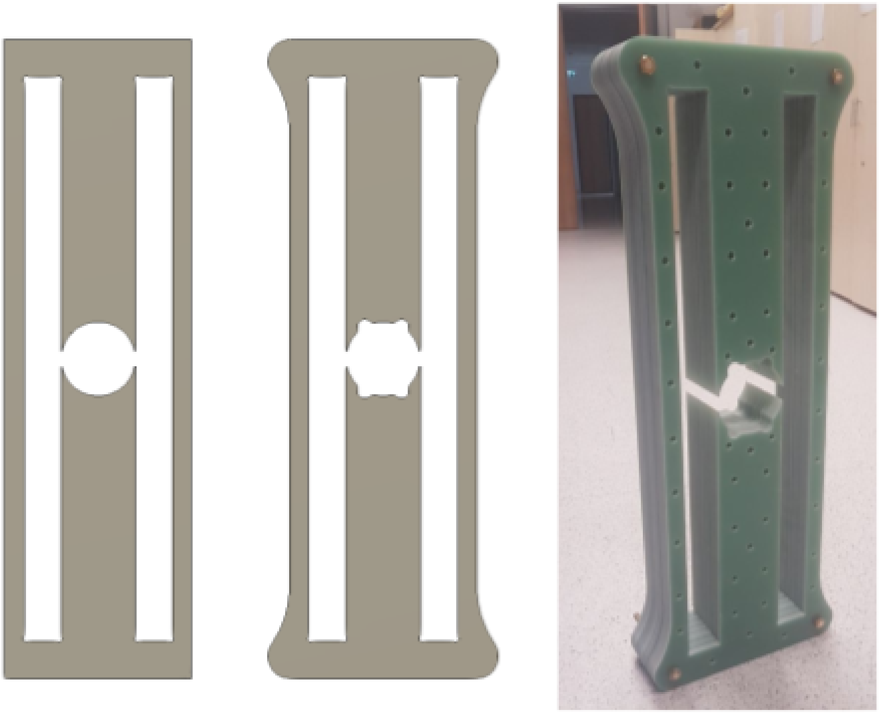

Figure 4.1: Left: Initial scanner body geometry. Center: Final scanner body geometry. Right: Assembled scanner body.

Due to their conductive and magnetic properties, using metals for the body is out of the question. For the material of the scanner body, G10 glass-fiber epoxy was chosen as a strong, non-conductive, and non-magnetic material. However, this material is very hard to come by in the thickness our design requires, which is 101 mm. Since there is hardly any shear load on the body, the body was instead built by stacking 20 layers of 5-mm sheets of G10 material. Bolts and nuts made out of brass were used to press and hold the layers together in four corners of the body. In Figure 4.1, the completed assembly of the scanner body can be seen. The holes that are left empty were later on utilized for securing individual magnets with bolts and caps from both ends.

4.2 Magnet Assembly

Due to the strong interactions among the magnets, it is not a trivial task to place the magnets into their targeted positions. Just as we needed a very strong body to keep the magnets in place, putting them in place also requires strength and control. The scanner body was cut with almost no tolerances so that an interference fit can hold the magnets in place with friction. While this approach makes sure that once the magnet is assembled it is secure for good, it also makes it even harder to assemble since once the magnet enters its slot, the friction has to be overcome as well as the magnetic forces acting upon the magnet. To manage this issue, a strategy needs to be formed and custom tools need to be built.

It is extremely hard to assemble the magnets together outside the body and put them in together, so they have to be put inside the body and locked in place one by one. When putting the magnets in one by one, the order in which they will be placed in matters due to their strong interaction. For clarity in explanation, magnets are numbered as such: Magnets 1 through 5 from top to bottom on the left column, and magnets 6 through 10 from top to bottom on the right column. With this numbering, magnet 1 is facing magnet 6, and magnet 2 is facing magnet 7, etc.

No matter the configuration, the first magnet is easy to place. However, starting with the second magnet, placing the magnets get increasingly more difficult. Magnets 1, 5, 6 and 10 are the corner magnets, and since they abut the upper and lower ends of the slots, their positions are easy to locate as well. Therefore, these corner magnets were placed in first, with the following order: 1, 10, 6, 5. Here, the second inserted magnet corresponds to the diagonal of the first inserted magnet to minimize the magnetic interaction. Once the corners are in place, next to come should be the magnets 3 and 8, that is, the center magnets. In the previous 4 magnets, we utilized the positional reference provided by the end of the slots, so it may be somewhat counterintuitive to not utilize the ends of the existing magnets in the same fashion. However, there is a problem with that approach and that is, until the magnets are fully in place and the cap is installed, the friction of the slot may not be enough to hold the magnet in place, and so even if we managed to push it into the right position, it would lose its position before locking in place. In contrast to that, once all four corner magnets are in place, the center magnets experience symmetrical force from the existing corner magnets so they are kind of self centering. Yet, simply the self centering force provided by the magnets can not be enough to correctly position the center magnets as the friction will prevent the magnet to come to an exact balance of forces. Therefore, dummy place holders with the exact shape and size of the magnets are 3D printed to temporarily put into the slots of magnet 2, 4, 7 and 9. By temporarily placing them in place, the positions of magnet 3 and magnet 8 are defined exactly. Once those magnets are placed and their positions are locked via caps, the dummy place holders are removed and the corresponding magnets (Magnet 2, 4, 7 and 9) are placed one by one. These last four magnets are the most challenging to insert as each of them are directly in contact with 2 of the magnets during insertion, which means that both the magnetic and frictional forces acting on them are tremendously large. Consequently, each magnet pushes out its own dummy place holder during insertion, making sure that the slot never remains empty. This precaution ensures that the previously placed magnets do not lose their positions.

Implementing this insertion strategy is far from trivial and requires a custom-made tool. Not only the magnets with identical poles facing each other repel one another, but they also desire to flip around so that opposing poles can face and attract each other. Such a flip can be very sudden, making the task of magnet insertion a safety hazard. Furthermore, once a magnet flips and gets attracted by other magnets, it is practically impossible to remove it. Therefore, it is extremely crucial that we never allow the magnets to flip during insertion. Overcoming this challenge requires a strong, tunnel-like structure, to guide the magnet insertion so that any rotation is constrained and rotation is only possible via the rotation of the entire guide structure. In the design of this custom tool, some of the previous material constraints such as non-conductivity does not apply since the tool will be used only during the assembly and not during operation. While any non-magnetic strong material is a good candidate, aluminum was chosen due to its availability and ease of use.

In this thesis, the guide structure was built using aluminum profiles that are normally designed for quick construction via standard connection systems, like LEGOs for engineering. Extruded out of dies, these aluminum profiles are very accurate in dimension, flat, and easy to find in various standard sizes.

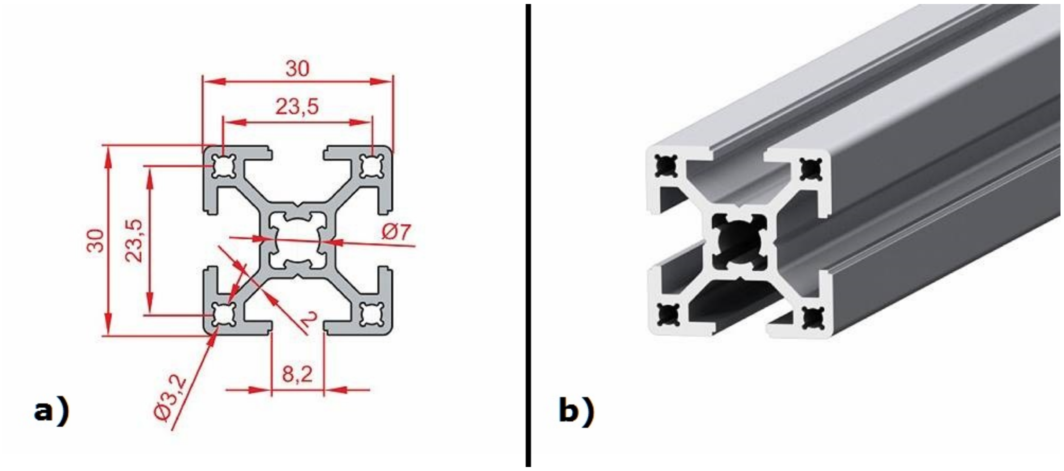

Figure 4.2: a) Cross section of the extruded aluminum profile. b) One such example of the aluminum profile.

In Figure 4.3a, the design of the guide structure is shown. The structure has a C shaped slot in it that accepts the scanner body and sits flush with it. Once the tunnel of the guide structure is aligned (first eyeballed manually and then aligned precisely with shims, using dummy place holders for test runs to check positioning accuracy and angular alignment) with the slot of the magnet, the guide structure and scanner body are secured together with clamps. Then, the insertion of the magnet is a matter of pushing it through the tunnel. In Figure 4.3b, how the guide structure fits over a magnet slot can be seen.

Despite using the guide structure, pushing the magnet in place is still a challenging task. While the magnet can initially be pushed down the tunnel manually with the help of a wooden stick, this method fails beyond a certain point as the magnetic forces exceed 2500 Newtons. Furthermore, the magnet's desire to flip exacerbates this problem by creating additional frictional forces between the magnet surface and the tunnel walls. To solve this challenge via a mechanical advantage, two different methods were utilized in this thesis. First, using car jacks was considered as a method to push the magnets into place. This method only worked for the early magnet placements and quickly proved to be unreliable. The next method was using a basic screw press, where a couple of identical aluminum plates were drilled in the same locations, and then a long bolt was put through the holes. The nuts were screwed onto the bolts from the outside of the plates. So, the plates were free to move away from the nuts, into the center, but the nuts blocked them from moving away in the opposite direction. Then, as the nuts are screwed on, the plates have to move closer and closer. By assembling the screw press around the magnet assembly and the guide structure, it can be made so that the aluminum plates push the magnet in as their nuts get screwed further. Due to the guide structure, the aluminum plates can not directly push on to the magnets, so wooden planks were inserted into the tunnel behind the magnet and the plates pushed onto the planks instead. Since the planks need to be inserted into the guide structure, the screw press needs to be able to move away considerably while not pressing. Usually, the longest bolt one can find is 1 meter long, which falls short for this task. Therefore, two 1 meter rods were connected together to make a 2 meter long rod using a special 50 mm long joining nut. In Figure 4.3c, the screw press can be seen in action while pushing the magnet through the guide structure.

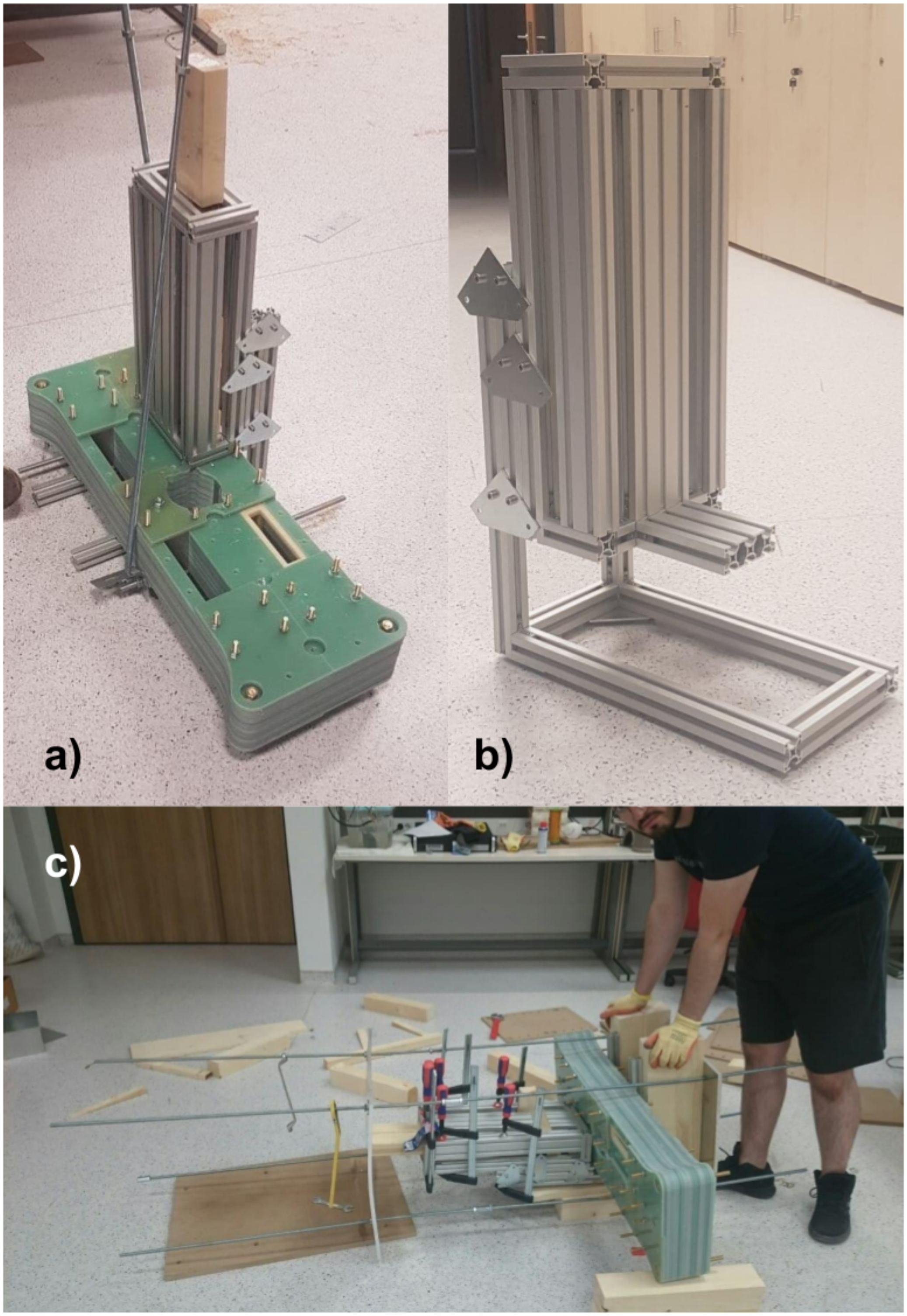

Figure 4.3: a) Guide structure positioned over a magnet slot. b) Guide structure made out of extruded aluminum profiles. c) A photograph taken during assembly of the magnet, screw press and guide structure can be seen in use. Notice how the aluminum plate bends due to the forces applied by magnets.

4.3 Shield

Once designed, the copper shield of the scanner is the easiest part to produce. A copper cylinder of approximately correct dimensions was bought, and it was machined to fit the design dimensions. Only the outer radius was left slightly oversized so that it can be filed and sanded in-house, until the shield fits very snugly into the bore with a friction fit. Woodworking clamps were used to push the finished shield into its final position.

4.4 Transmit Coil

The construction of the transmit coil is primarily focused on the former geometry and winding. There are few points regarding the transmit coil that requires attention during the planning and construction stages. First, the coil former should be constructed so that it can be easily positioned at the correct location in the scanner. Second, there may be points in the multi-layered coil that are physically very close, yet experience large potential differences. High voltage arcs between those points should be avoided. Third, it must be ensured that there is a path for heat to escape, since the material used in building the former is not resistant to heat and has poor thermal conductivity.

To address the first issue, we either have to glue the parts down in their place after positioning them carefully, or we have to design the geometries so that they have features designed to abut other, stationary parts. As glue method is irreversible and messy, we chose to go with the second method. For this end, we need a stationary reference feature (e.g., a specific point or an entire surface) on the scanner, which can be either the body of the scanner or the shield, which is press fitted into its place and practically fixed to the body. As it is closer and easier, we utilised the front face of

Figure 4.4: Copper shield of the scanner, ready to insert.

the copper shield as the reference surface. Since the transmit coil is axisymmetrical, and its former's outer diameter fits the inside diameter of the shield, only the position along the z-axis needs to be referenced. Therefore, we utilised simple tabs that stop the former from moving further than its intended position. The shape of the tabs and how they mate with the copper shield can be seen in Figure 4.5a

To address the second issue, which is the risk of arcs forming between layers, we used Kapton tape to secure the coil as we wind them. Kapton is a polyimide film that provides electrical and thermal insulation. It also features a high dielectric strength, effectively increasing the breakdown voltage between the layers. Some form of adhesive or tape has to be used to secure the windings of the coil, so using a dielectric Kapton tape does both duties at once.

To address the third issue, which is the heating of the coil, ducts were provided on both faces of the former so that air flow is not prevented. These ducts also function as paths for the ends of the coil wires that need to be connected to the amplifier and matching circuit.

In Figure 4.5b, the finalised model of the transmit coil former can be seen.

4.5 Doubly Tunable Gradiometric Receive Coil

In Section 3.6, the design procedure of the receive coil was detailed. As mentioned in that section, the coarse tuning segment moves the fine tuning segment with it, however, the fine tuning segment can also move when the coarse tuning segment is stationary. The opposite case (i.e., coarse tuning segment moves but the fine tuning stays stationary) should be prevented. This requirement creates the main challenge with the mechanical design and construction of the receive coil. The movement of the segments are controlled with fine pitched threaded screws and this behavior

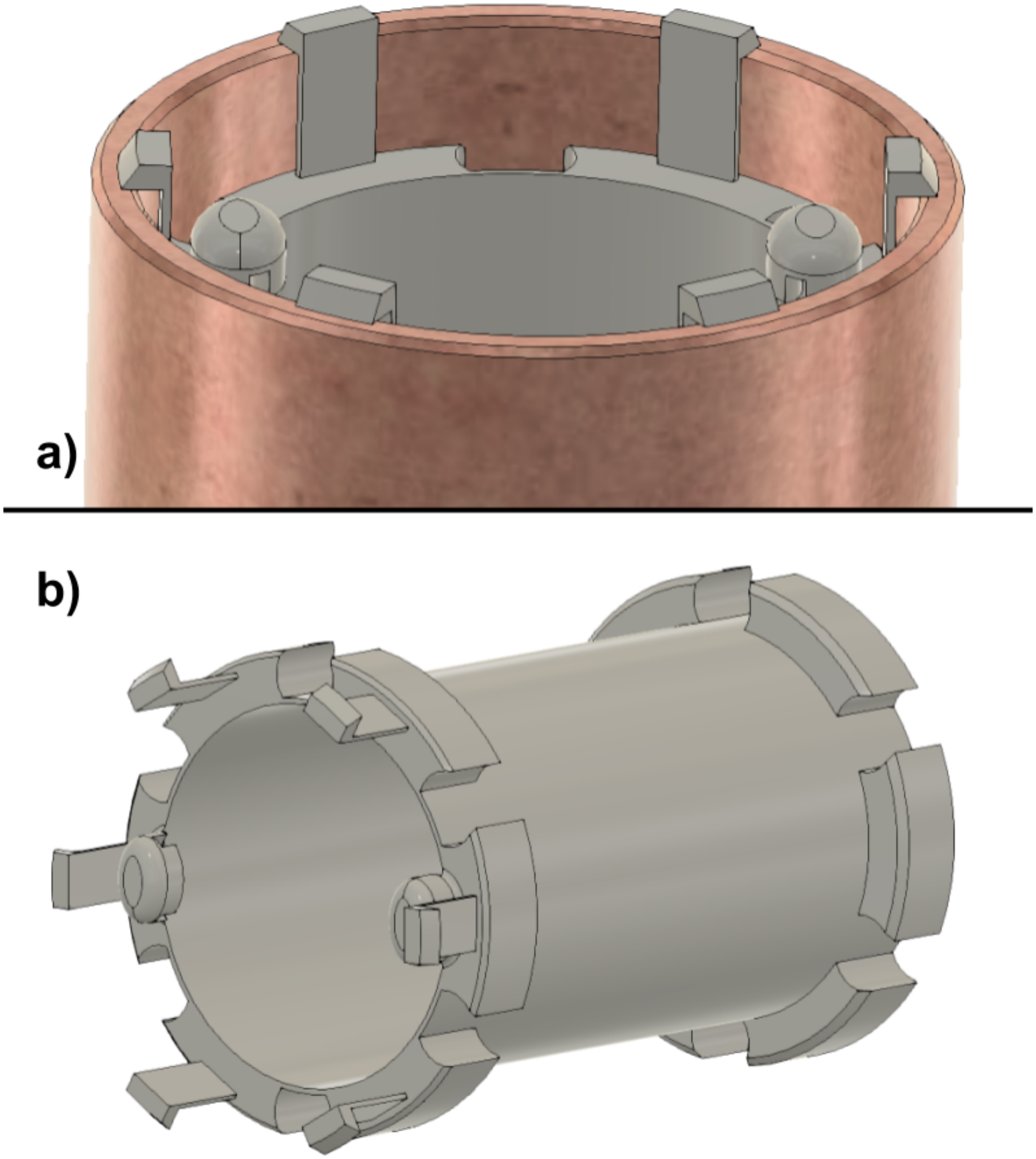

Figure 4.5: a) Tabs that define the position of the transmit coil former along the z-axis. Thin base of the tabs are flexible and can flex inwards when the former is inserted from the other end. Only one end of the former has these tabs so that the coil can be removed when desired. b) Finished design of the transmit coil former.

dictates that the fine tuning screw should move the fine tuning segment in relation to the coarse tuning segment and not the stationary body. To achieve this mode of operation, both tuning segments need to have nuts that mate with screws attached on to them, however, these nuts need to be attached to the segments from outside the bore to not hinder imaging. Since the fine tuning segment completely blocks the coarse tuning segment's access to the outside, and any protrusion from the body of the segment would prevent the winding of the coil, a separate part that has the nut attached must be fixated on to the windings of the coarse tuning segment after it is wound. In Figure 4.6, several images of the mechanism and how it is put together are shown to clarify the working mechanism. In this figure, the gray colored part is the core part of the former that holds the central segment and the stationary side segment of the receive coil. The yellow colored part is the part that the coarse tuning windings are wound onto. This part moves in the z-axis by sliding over the grey part. The green colored part is the part that carries the fine tuning windings. It abuts the yellow part and similarly slides over the grey part. It has a tab that has a hole for the plastic screw and holds a plastic nut from behind to be actuated by a screw. The screw that goes into the hole pushes onto the blue part shown in the last step. The red part and the yellow part are glued onto the coarse tuning windings, which allow the red part's tab to move the coarse tuning segment. The red part's screw pushes onto the side of the swap coil, which is stationary. Therefore, the red part, which is glued to the coarse tuning segment, is positioned with respect to the stationary scanner via its screw. On the other hand, the green part which holds the fine tuning windings is positioned with respect to the coarse tuning segment via its screw.

4.6 Swap Coil

Unlike the axisymmetric transmit coil, the swap coil is designed with a specific orientation, therefore one of the requirements driving the design of its former is that

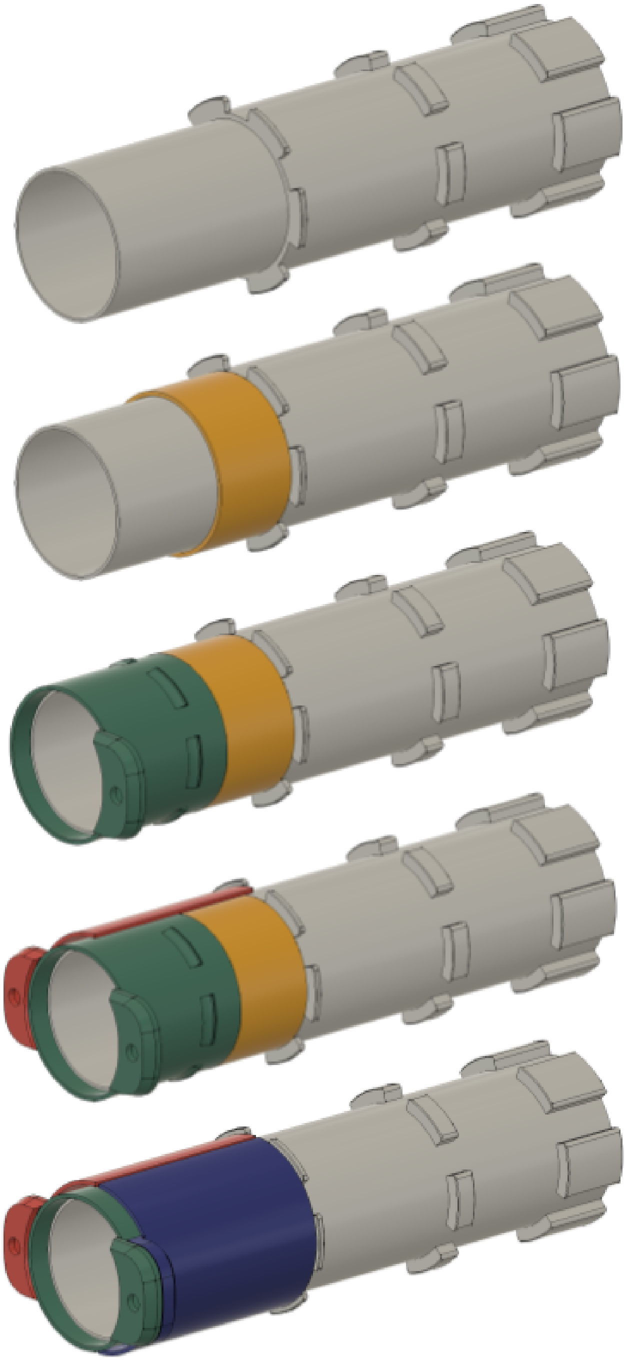

Figure 4.6: Construction steps of the receive coil former, displayed one piece at a time from top to bottom. Yellow: Coarse tuning segment's carrier. Green: Fine tuning segment's carrier, which also holds a plastic nut to mate with the fine tuning screw. Red and blue: Glued onto the yellow part and the windings on it to transfer force from the adjustment mechanism. The red part also holds a plastic nut to mate with the coarse tuning screw.

it should not rotate in the bore. Another requirement is that the former should be able to keep the coil in shape. This requirement is actually non-trivial since the shape of the coil does not allow it to be held simply by tension. Any tension on the wire tries to pull it on to a flat plane instead of the curved surface it needs to occupy. Therefore, the former geometry needs to prevent the coil from flattening.

To address the first issue, the former was designed to have channels built on both sides that serve as a cooling duct as well as a rotational reference point that can be made to mate with a stationary body to prevent rotation. To address the second issue, a mushroom like extension was added to the radial column that the coil winds around. In Figure 4.7, both of these features can be seen.

4.7 Robot Arm

A robot arm (Velmex X-Slide) was responsible for positioning the object inside the free bore of the scanner. When installing the robot arm, care must be taken to position it so that its coordinate system aligns well with the coordinate system of the scanner. If not, a rotation may be introduced into all the scans and measurements utilising the robot arm. In fact, in Figure 3.4c, it can be seen that, the measured B_z component has a slight slope to it while in theory it should have been entirely zero. This error is due to the z-axis of the robot arm not being perfectly aligned with the z axis of the magnet. A very slight misalignment of the y-axis can be seen in Figure 3.4d as well.

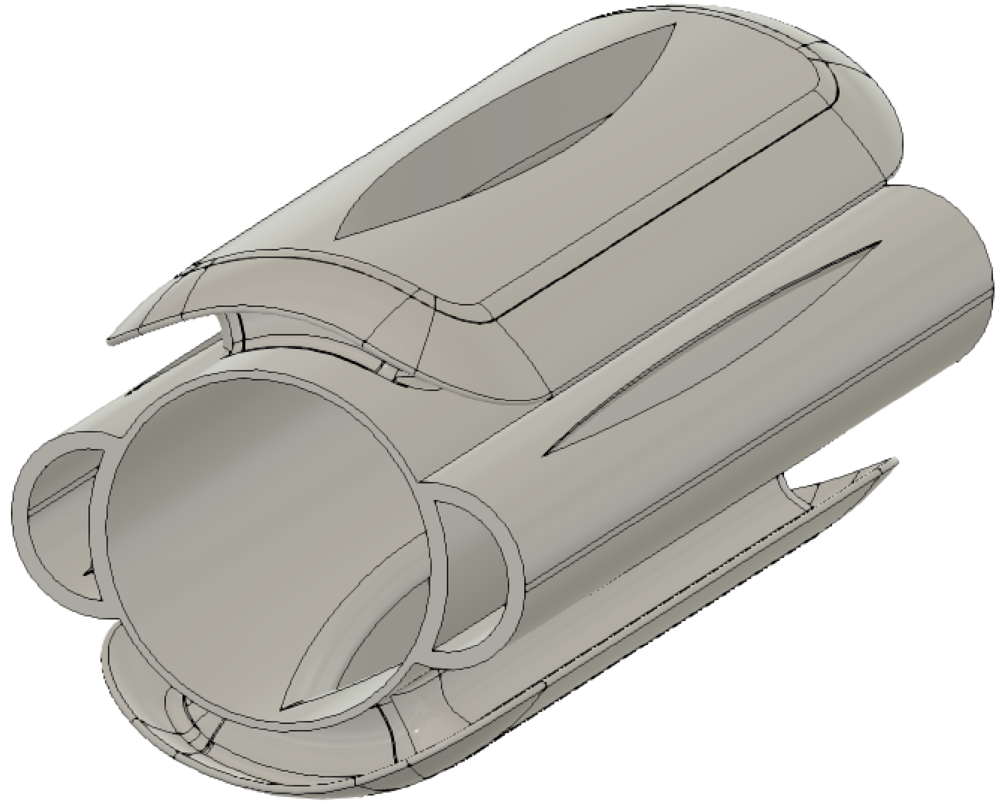

Figure 4.7: Former of the swap coil. The two channels on the sides of the body serve as ducts to let air flow onto the coil that would otherwise have no contact with the outside. They also prevent some reference point to lock the rotation of the swap coil. The columns on the top and bottom of the former provide the support for the coil. Mushroom like extension of the columns prevent coil from flattening into a plane and unwinding.

Chapter 5

Results

5.1 Selection Field

All three components of the SF were measured on a 3D grid with the gaussmeter in the setup described in Section 3.1. Then, the gradients G_{xx}, G_{yy} and G_{zz} were calculated from the measured flux densities. Presented in Figure 5.1 is the measured field gradients along center lines (e.g., $y = z = 0$ line for G_{xx}, etc.) for each axis. G_{xx} measures approximately -4.4 T/m at $x = 0$ and G_{zz} measures approximately 4.4 T/m at $z = 0$. They have the same magnitude but opposite signs as expected. The measured G_{yy} is quite close to but not exactly zero in magnitude. This slight offset may be due to the misalignment problem mentioned in Section 4.7. It can be seen that the gradients are not constant over the entire range, but the variations are small and do not hinder imaging experiments. These inhomogeneities may cause a slight warping artifact, but there exists a method for unwarping them [20].

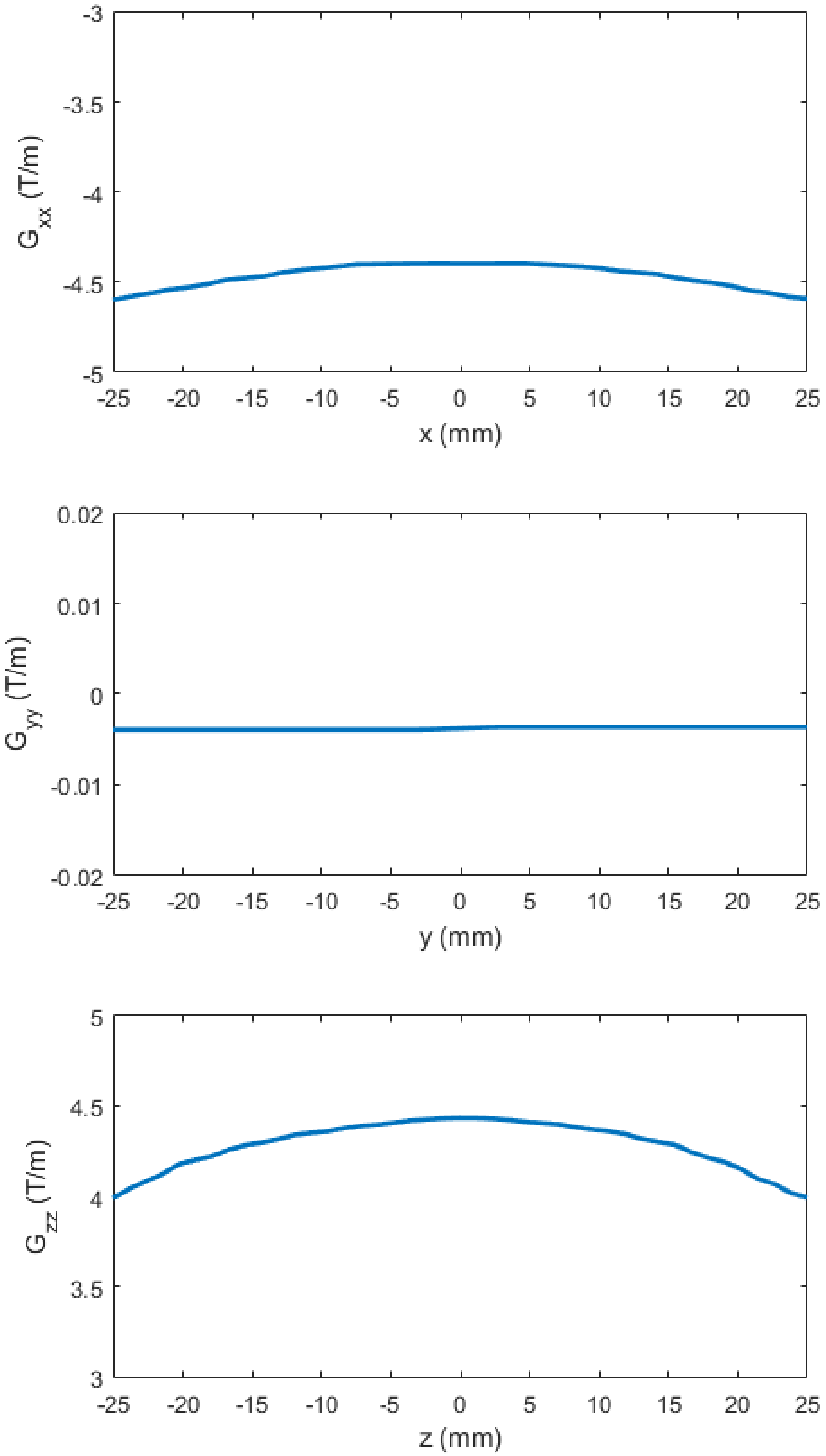

Figure 5.1: Top: G_{xx} along x-axis. Middle: G_{yy} along y-axis. Bottom: G_{zz} along z-axis.

5.2 Simulation Results

To confirm that the swap coil works as intended and that the design methodology is correct, an imaging simulation was done. To this end, a virtual phantom that has multiple layers of text written with SPIO nanoparticles was designed. When the phantom is imaged in projection format across the layers, none of the layers are legible since the image is a superposition of each layer. When imaged in slices by volumetric acquisition, however, the individual layers can be resolved. The virtual phantom and its projection along the FFL direction can be seen in Figure 5.2. The top layer of the phantom reads “TOP”, the middle layer of the phantom reads “MID” and the bottom layer of the phantom reads “BOT”. The layers have a thickness of 5 mm, and they are separated by 5 mm distances each. So, the centers of the layers are 10 mm apart. The phantom is approximately 2-cm wide and 8-cm long.

Then, using the coil sensitivity matrices acquired from COMSOL simulations, the scanner designed in this thesis is mimicked in simulation with the following parameters: The particle diameter was 25 nanometers, the drive field frequency was 25 kHz, and simulation sampling rate was 500 times the drive field frequency. In the simulation, both projection images (i.e., swap coil current is zero, FFL-mode) and volumetric images (swap coil in operation, FFP-mode) from several slices are acquired. In Figure 5.3, projection MPI image of the virtual phantom is shown alongside the projection of the phantom. It can be seen that none of the layers are legible. It can also be observed that a higher intensity is achieved at points where particles from different layers are aligned.

Following the projection results, in Figure 5.4, volumetric acquisition results are presented. Volumetric images from each layer of the phantom are acquired, and they clearly show that each layer is resolved individually. This result confirms that the swap coil can operate as intended and the methodology is sound.

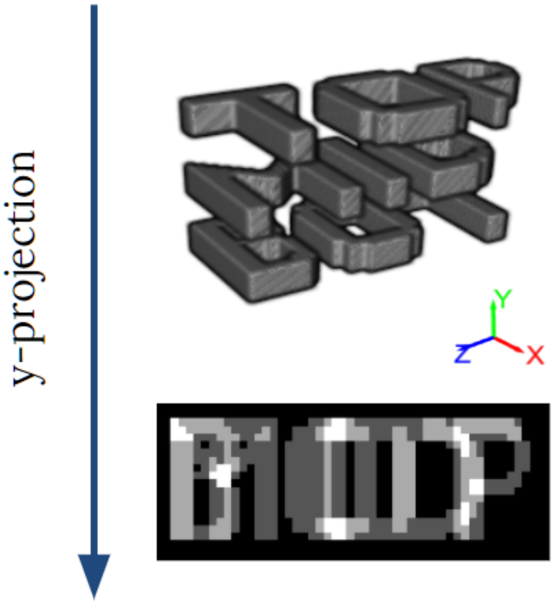

Figure 5.2: Virtual phantom that is prepared for imaging simulations. It consists of three layers that read “TOP”, “MID” and “BOT”, from top to the bottom, respectively.

5.3 Experiment Results

After the construction of the scanner was completed and the scanner was ready to use, a point source phantom was prepared to acquire a projection image. The phantom is prepared by filling a short section of a 2-mm inner diameter capillary tube with 5 times diluted Perimag SPIO nanoparticles (Micromod GmbH, Germany). Then, both ends of the tube was sealed with hot glue, inserted into a 3D printed apparatus held by the robot arm, and further sealed by wrapping parafilm (Bemis Company, Neenah, WI) around it. Once the phantom was ready, a projection image was acquired by individually acquiring 847 partial field of views (pFOV) in total, configured in 11 lines along the bore, each consisting of 77 pFOVs. In Figure 5.5,

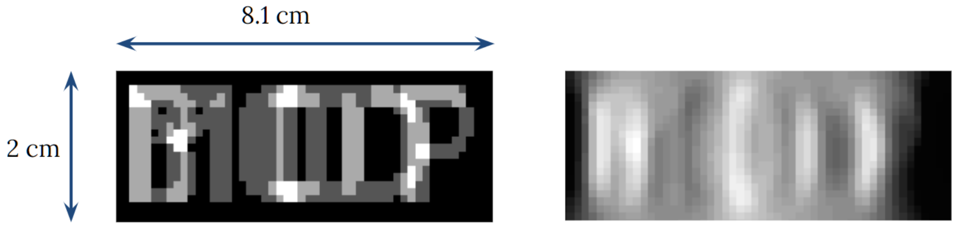

Figure 5.3: Left: Projection of the phantom along y-axis. Right: Projection MPI image of the phantom. Two observations can be made: One is that individual layers are not resolved, and the other is that image intensity is higher at points where particles from different layers are aligned.

the acquired image can be seen after it is reconstructed.

After the point source phantom was imaged, a spiral phantom was prepared with a 1.25-mm inside diameter capillary tube and 5 times diluted Perimag, and then imaged with the scanner. In Figure 5.6, prepared phantom can be seen, along with the projection image acquired from it. The shape of the spiral is resolved very clearly, showing that the scanner can provide useful "bright blood" images of aorta and main veins of mice.

Both the asymmetrical point source phantom image and the distortion near the edge of the spiral phantom image hint that point spread function of the scanner is not isotropic. This anisotropy is to be expected, as the resolution in x-space reconstructed images is better along the direction of the drive field (z-direction in this case). Further experimental analysis needs to be done to create a map of the point spread function variation over the scanner bore volume. It is clear that any existing variation is small enough to not hinder qualitative analyses of the imaging subject, although any quantitative results would be effected.

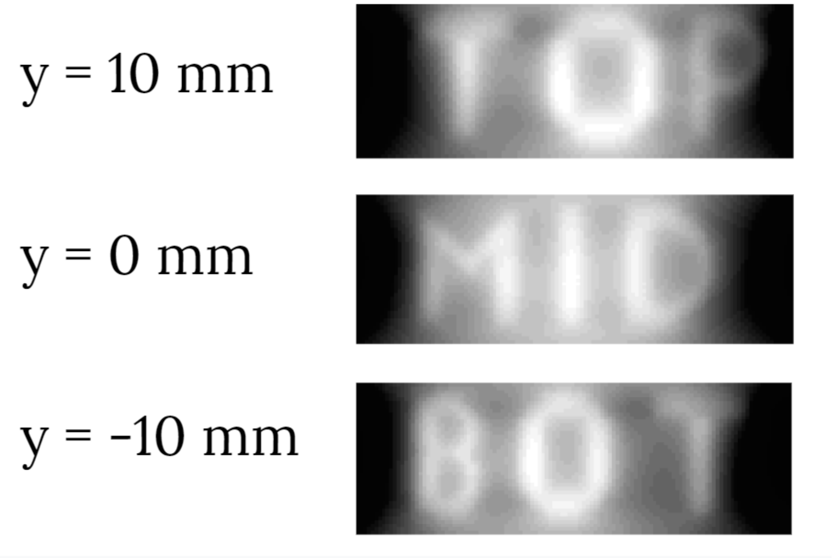

Figure 5.4: Top: Volumetric image acquired from y = 10 mm slice, text “TOP” is clearly legible and resolved. Middle: Volumetric image acquired from y = 0 mm slice, text “MID” is clearly legible and resolved. Bottom: Volumetric image acquired from y = -10 mm slice, text “BOT” is clearly legible and resolved. There is some background hazing in the images, probably due to the point spread function of the system.

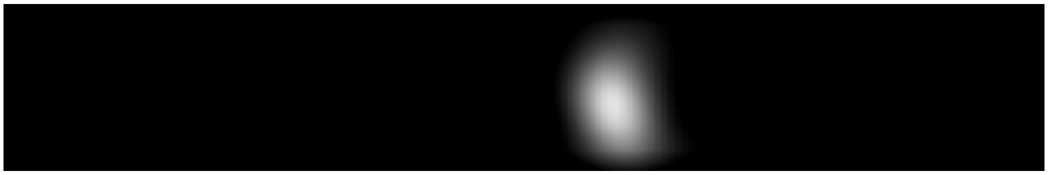

Figure 5.5: First projection image of a point source phantom acquired with the scanner. Imaged phantom consists of a 5 times diluted Perimag sample that is contained inside a 2-mm wide capillary tube. Full width half max dimensions of the acquired image of phantom is 3 mm along the z-direction and 5 mm along the x-direction.

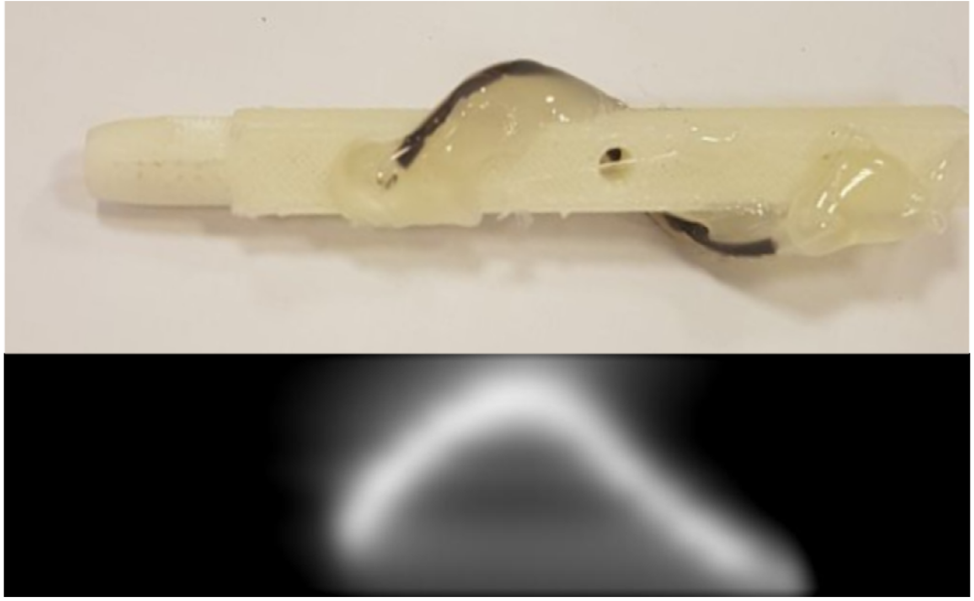

Figure 5.6: Top: Spiral phantom prepared by wrapping a 5x diluted Perimag filled, 1.25-mm inner diameter capillary tube around a 3D printed sample holder part. Ends of the capillary tube was capped with hot glue to prevent SPIO leakage. Furthermore, the phantom was wrapped in Parafilm to ensure no nanoparticle leaks can occur inside the scanner. Bottom: Projection image acquired from the spiral phantom.

Chapter 6

Discussion and Conclusion

6.1 Flipping the FFL Horizontally

A feature of the swap coil that was not discussed in detail is that, when the current direction is reversed, it can flip the existing FFL SF horizontally, meaning that an FFL can be generated along the x-axis. This behavior was not well examined and therefore only discussed in this section. However, it may prove useful in a future work, as such an ability would mean that the projection images from two directions may be acquired instead of one. Complementing a “localizer” projection scan along the y-axis with another one along the x-axis may prove useful in practical applications.

6.2 Individual Driving of Swap Coil Halves

In this thesis, the swap coil was designed and operated as a single coil, meaning that the top and bottom halves of it were in series. This approach makes sure that both halves have the exact current going through them, simplifying the design. However, at the cost of a second amplifier and another DAQ channel, the top and bottom halves of the swap coil can be driven individually to serve additional functions. When driven symmetrically, the swap coil generates the FFP at y=0. However, by driving it asymmetrically, the FFP position can be controlled in the vertical direction. Such a function can render the y-axis of the robot arm unnecessary. Another function gained is the ability to generate a constant gradient within the entire bore. By changing the current direction in only one of the halves, swap coil can be operated in constant gradient mode. By aligning the swap coil horizontally instead of vertically, a constant gradient can move the existing FFL along x-direction, potentially eliminating the need for x-axis of the robot arm in projection imaging experiments.

6.3 Conclusion

Currently there exists no hybrid, dual-mode MPI scanners that can utilise the benefits of both FFP and FFL topologies. This thesis demonstrates the potential for such a hybrid scanner and presents a method for designing and constructing each component of it in detail. As shown in Section 5.2, the proposed approach is capable of enabling an FFL MPI scanner to perform volumetric acquisition in FFP mode. Such an ability allows for “localizer” scans to be performed prior to defining a region of interest for volumetric acquisition. Such a practice is routine in MRO protocols and availability of it will surely prove useful in MPI, as well. Owing to its 36-mm diameter bore, preclinical studies can be done with this scanner on mice, which is a capability our research center did not possess before.

Bibliography

[1] Bernhard Gleich and Jürgen Weizenecker. "Tomographic imaging using the nonlinear response of magnetic particles". In: *Nature* 435.7046 (2005), pp. 1214–1217. DOI: `10.1038/nature03808`.

[2] Yi-Xiang J Wang. *Current status of superparamagnetic iron oxide contrast agents for liver magnetic resonance imaging.* Dec. 2015. URL: `https://www.ncbi.nlm.nih.gov/pmc/articles/PMC4679775/`.

[3] I Molwitz et al. "First magnetic particle imaging angiography in human-sized organs by employing a multimodal ex vivo pig kidney perfusion system". In: *Physiological Measurement* 40.10 (Oct. 2019), p. 105002. DOI: `10.1088/1361-6579/ab4436`. URL: `https://doi.org/10.1088%5C%2F1361-6579%5C%2Fab4436`.

[4] Xinyi Y Zhou et al. "Magnetic particle imaging for radiation-free, sensitive and high-contrast vascular imaging and cell tracking". In: *Current Opinion in Chemical Biology* 45 (2018). Molecular Imaging / Chemical Genetics and Epigenetics, pp. 131–138. ISSN: 1367-5931. DOI: `https://doi.org/10.1016/j.cbpa.2018.04.014`. URL: `http://www.sciencedirect.com/science/article/pii/S136759311830005X`.

[5] J Weizeneceker, J Borgert, and Bernhard Gleich. "A simulation study on the resolution and sensitivity of magnetic particle imaging". In: *Physics in*

Medicine and Biology 52.21 (Oct. 2007). DOI: `https://doi.org/10.1088/0031-9155/52/21/001`.

[6] Patrick W Goodwill and Steven M Conolly. "The X-Space Formulation of the Magnetic Particle Imaging Process: 1-D Signal, Resolution, Bandwidth, SNR, SAR, and Magnetostimulation". In: *IEEE Transactions on Medical Imaging* 29.11 (2010), pp. 1851–1859. DOI: `10.1109/tmi.2010.2052284`.

[7] Juergen Weizenecker, Bernhard Gleich, and Joern Borgert. "Magnetic particle imaging using a field free line". In: *Journal of Physics D: Applied Physics* 41.10 (Jan. 2008), p. 105009. DOI: `10.1088/0022-3727/41/10/105009`.

[8] Edward P Furlani. *Permanent magnet and electromechanical devices: materials, analysis, and applications*. Academic press, 2001.

[9] Emil Lenz. "Ueber die Bestimmung der Richtung der durch elektrodynamische Vertheilung erregten galvanischen Ströme". In: *Annalen der Physik und Chemie* 107.31 (1834), pp. 483–494. DOI: `10.1002/andp.18341073103`.

[10] P. W. Goodwill et al. "Projection X-Space Magnetic Particle Imaging". In: *IEEE Transactions on Medical Imaging* 31.5 (2012), pp. 1076–1085. DOI: `10.1109/tmi.2012.2185247`.

[11] Mustafa Utkur and Emine Ulku Saritas. "Comparison of different coil topologies for an MPI relaxometer". In: *2015 5th International Workshop on Magnetic Particle Imaging (IWMPI)* (Mar. 2015). DOI: `https://doi.org/10.1109/IWMPI.2015.7107082`.

[12] P. Karp and D. Duret. "Unidirectional magnetic gradiometers". In: *Journal of Applied Physics* 51.3 (1980), pp. 1267–1272. DOI: `10.1063/1.327819`. eprint: `https://doi.org/10.1063/1.327819`. URL: `https://doi.org/10.1063/1.327819`.

[13] Zhi Wei Tay et al. *A High-Throughput, Arbitrary-Waveform, MPI Spectrometer and Relaxometer for Comprehensive Magnetic Particle Optimization and Characterization*. Sept. 2016. URL: `https://www.ncbi.nlm.nih.gov/pmc/articles/PMC5043240/`.

[14] B. Zheng et al. "Optimal Broadband Noise Matching to Inductive Sensors: Application to Magnetic Particle Imaging". In: *IEEE Transactions on Biomedical Circuits and Systems* 11.5 (2017), pp. 1041–1052. DOI: `10.1109/TBCAS.2017.2712566`.

[15] *LFR Current Probe*. URL: `http://www.pemuk.com/products/lfr-current-probe.aspx`.

[16] F. Bonetto, E. Anoardo, and M. Polello. "Saddle coils for uniform static magnetic field generation in NMR experiments". In: *Concepts in Magnetic Resonance Part B: Magnetic Resonance Engineering* 29B.1 (2006), pp. 9–19. DOI: `10.1002/cmr.b.20057`.

[17] URL: `https://aetechron.com/IND-RESEARCH-7796.shtml`.

[18] M. Utkur, Y. Muslu, and E. U. Saritas. "Relaxation-based color magnetic particle imaging for viscosity mapping". In: *Applied Physics Letters* 115.15 (2019), p. 152403. DOI: `10.1063/1.5110475`. eprint: `https://doi.org/10.1063/1.5110475`. URL: `https://doi.org/10.1063/1.5110475`.

[19] URL: `https://aetechron.com/IND-RESEARCH-7224.shtml`.

[20] Ecrin Yagiz, Ahmet R Cagil, and Emine Ulku Saritas. "Non-ideal selection field induced artifacts in X-space MPI". In: *International Journal on Magnetic Particle Imaging* 6.2 (2020).